

PHUMA: Physically Reliable Humanoid Locomotion Dataset

Kyungmin Lee^{1*} Sibeon Kim^{1*} Youngdo Lee¹ Minho Park¹ Hyunseung Kim¹
 Dongyoon Hwang¹ Donghu Kim¹ Hojoon Lee¹ Jaegul Choo¹
¹KAIST
 {kmllee, bioceo78}@kaist.ac.kr

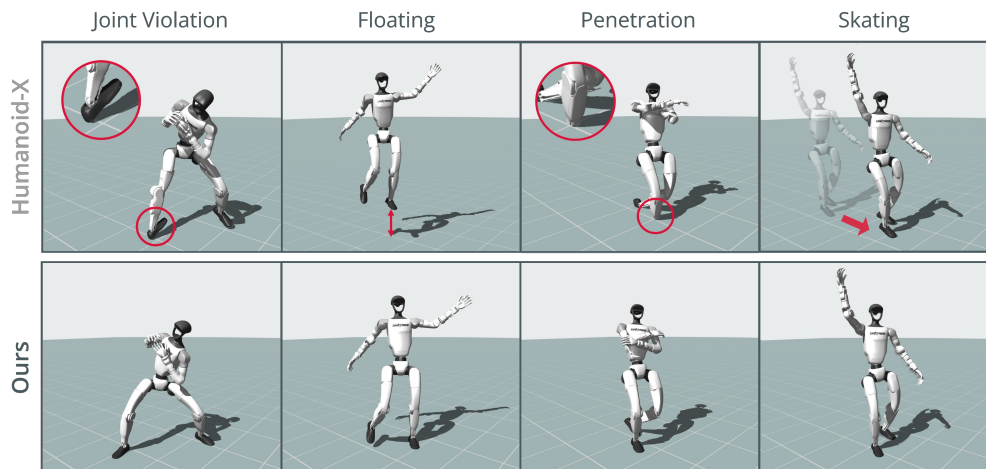


Figure 1: **Physical Reliability of Humanoid-X vs. PHUMA.** Each column illustrates four failure modes: joint violation, floating, penetration, and skating. Humanoid-X [1] (top row) often exhibits these issues due to direct video-to-motion conversion, while PHUMA (bottom row) mitigates those violations through careful data curation and physically reliable retargeting.

Abstract: Motion imitation is a promising approach for humanoid locomotion, enabling agents to acquire humanlike behaviors. Existing methods typically rely on high-quality motion capture datasets such as AMASS, but these are scarce and expensive, limiting scalability and diversity. Recent studies attempt to scale data collection by converting large-scale internet videos, exemplified by Humanoid-X. However, they often suffer from physical artifacts such as floating, penetration, and foot skating, which hinder stable imitation. To address this, we introduce **PHUMA**, a **Physically Reliable HUMANoid** locomotion dataset produced by a two-stage pipeline combining physics-aware curation and physics-constrained retargeting, aggregating both motion capture and internet video into a physically reliable, 73-hour corpus. On motion tracking benchmarks, PHUMA-trained policies achieve higher success rates than those trained on AMASS and Humanoid-X, and successfully transfer zero-shot to a real Unitree G1. The code is available at <https://davian-robotics.github.io/PHUMA>.

1 Introduction

Humanoid robots are a key step toward general-purpose embodied AI, but deploying them in the real world first requires reliable and natural locomotion. While reinforcement learning (RL) with task-oriented rewards (e.g., velocity tracking) has driven remarkable progress in quadrupedal locomotion [2–4], applying it to humanoids often yields gaits that are effective yet non-humanlike [5, 6],

*Equal Contribution

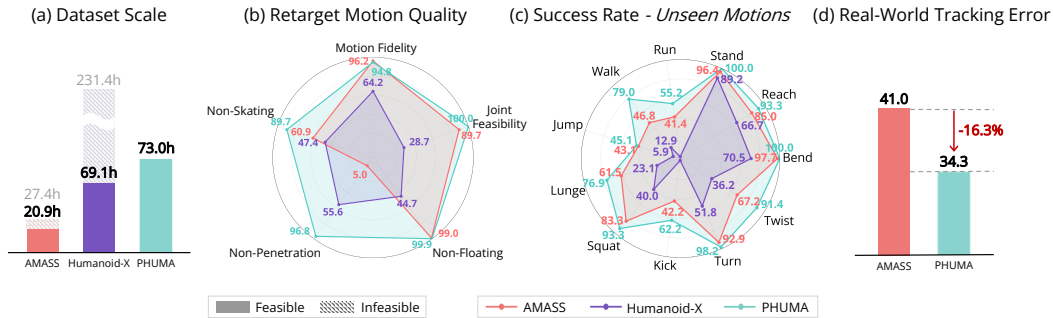


Figure 2: **Overview of datasets and performance.** (a) Composition of feasible and infeasible human motion sources in each dataset. (b) Physical reliability of each dataset; AMASS is retargeted using a standard learning-based inverse kinematics method. (c) Success rate on unseen motions. (d) Motion tracking error on real Unitree G1.

since such rewards struggle to capture natural whole-body coordination. To address this limitation, motion imitation has emerged as a promising paradigm, where policies are trained to replicate human movements through a three-stage pipeline: (1) collecting human motion data, (2) retargeting it to the robot’s morphology, and (3) tracking the retargeted trajectories with RL [7–11].

Despite its promise, progress in motion imitation is fundamentally constrained by the scale, diversity, and physical feasibility of human motion data. High-quality motion capture datasets such as LaFAN1 [12] and AMASS [13] provide a high proportion of physically feasible motions, but are limited in scale and diversity, with content dominated by simple motions such as reaching and walking. To overcome this scarcity, recent work has sought to scale data collection by leveraging vast internet videos. Humanoid-X [1] exemplifies this trend by converting videos to SMPL representations [14, 15] using a video-to-motion model [16], then retargeting them to humanoid embodiments. However, this pipeline suffers from two types of physical violations. First, the video-to-motion model often misestimates global translation, producing artifacts such as floating or ground penetration. Second, the retargeting stage prioritizes joint alignment over physical plausibility [9, 17], leading to joint violation and foot skating as illustrated in the top row of Figure 1.

In response, we introduce **PHUMA**: a **Physically Reliable HUMANoid** locomotion dataset that scales internet video into a high-quality training corpus by jointly filtering infeasible motions and enforcing physical constraints during retargeting. As illustrated in Figure 3.1, we first collect large-scale, diverse human motion data and filter out infeasible motions from Humanoid-X, such as root jitter or actions requiring external objects like sitting on chairs. As shown in Figure 3.2, we then apply Physically constrained Shape-adaptive Inverse Kinematics (PhySINK), enforcing soft joint limits, ground contact, and anti-skating constraints to eliminate violations like joint over-extension, floating, and sliding. As a result, PHUMA offers the most physically feasible motion among existing datasets: 73.0h total, $3.5\times$ that of AMASS and exceeding Humanoid-X’s 69.1h (out of 231.4h).

To validate its effectiveness, we evaluate PHUMA across four axes: (i)-(ii) whether physics-aware curation and PhySINK retargeting contribute to downstream motion tracking, (iii) comparison against existing datasets, and (iv) zero-shot deployment on a real Unitree G1. We use the Masked-Mimic [8] for in-simulation tests on both Unitree G1 and H1-2 humanoids, and BeyondMimic [18] for real-world deployment on a Unitree G1. On 504 self-recorded videos across 11 motion types, policies trained with PHUMA outperform both AMASS and Humanoid-X across all motion types in success rate (Figure 2(c)). Furthermore, on 24 motions sampled from the PHUMA test set (6 per category: stationary, angular, vertical, and horizontal), the PHUMA-trained policy achieves 16.3% lower tracking error than the AMASS-trained policy in the real world (Figure 2(d)).

2 Related Work

PHUMA focuses on constructing a large-scale, physically reliable humanoid locomotion dataset, requiring two components: (1) collecting diverse human motion data and (2) retargeting it to the humanoid robots.

2.1 Human Motion Data

Human motion data, typically in the SMPL format [14, 15], comes from two main sources: motion capture (mocap) and video-based reconstruction. Mocap [19–21] provides accurate kinematics but demands expensive instrumentation and studio effort. LaFAN1 [12], for instance, offers high fidelity but only a few hours of motion, while AMASS [13] unifies many mocap datasets yet remains walking-centric, limiting diversity. Concurrent work such as Bones-SEED [22] scales open mocap data through commercial studio production. Driven by advances in video-to-motion recovery [16, 23–26], human video has emerged as a scalable, diverse alternative. Recent works [27–36] leverage this scalability and diversity, with Humanoid-X [1] notably providing abundant data from the Internet. However, video-derived motions often exhibit severe jitter across frames and physical artifacts such as foot sliding or ground penetration [37–42]. To mitigate these artifacts, recent methods employ automated filtering, either by discarding motions a pretrained tracking policy cannot reproduce in simulation [11], or by detecting foot-ground contacts through hand-tuned thresholds (e.g., zero-velocity and ankle-height) [10]. Yet, the former risks rejecting feasible but out-of-distribution motions, and the latter misjudges contact when video-estimated global translation is noisy. In contrast, PHUMA applies a physics-aware curation pipeline over both motion capture and human video, discarding only severely corrupted motions while correcting recoverable physical violations, such as implausible foot-ground contact, during retargeting.

2.2 Humanoid Motion Retargeting

Building on its success in physics-based character control [7, 8, 37, 43–48], human motion data is increasingly adapted for humanoid robotics [10, 18, 49–61]. This requires motion retargeting [62], mapping human motions onto robots that share a humanoid topology but differ in kinematics and body proportions [63–65]. Standard Inverse Kinematics (IK) methods [66–68] are widely adopted for their simplicity, but they often ignore these morphological differences, leading to unnatural artifacts such as misaligned foot orientations. While approaches like GMR [69] demonstrate that careful engineering can improve IK outcomes, they still rely heavily on heuristic scale adjustments and remain prone to floating artifacts. To explicitly address shape discrepancies, Shape-adaptive Inverse Kinematics (SINK) methods [9, 17, 70–72] adapt the human body shape to the robot before pose alignment, which is effective at pose matching but physically under-constrained. To enforce physical realism, several works [73–78] add contact constraints, but assume clean motion where the ground follows from the lowest foot position; on noisy video-derived motion this collapses, flagging nearly every frame as floating. Neural retargeting [79, 80] learns the mapping from data, yet still needs a prior retargeting method for training pairs. To bridge these gaps, we propose Physically constrained Shape-adaptive Inverse Kinematics (PhySINK), which augments SINK with joint feasibility, grounding, and anti-skating terms. The bottleneck is contact estimation: rather than relying on the lowest foot position, we derive robust contact signals through our physics-aware curation, which estimates the ground plane by majority voting. This lets PhySINK perform precise, physically reliable retargeting even on in-the-wild video, ultimately forming PHUMA.

3 Method

Our goal is to construct PHUMA, a large-scale, physically reliable dataset for humanoid locomotion. We build upon the Humanoid-X motions [1], which are rich in scale but exhibit physical artifacts. We first apply physics-aware curation to filter out problematic motions (Section 3.1). Next, to address artifacts introduced during the retargeting process itself, we employ PhySINK, our physics-constrained retargeting method that adapts the curated motion to the humanoid while enforcing physical reliability (Section 3.2). Our full pipeline is illustrated in Figure 3.

3.1 Physics-Aware Motion Curation

Our curation pipeline addresses three key artifacts in raw motion data: severe jitter, physical instability from interactions with objects absent in the humanoid’s environment (e.g., chairs), and incorrect foot-ground contact (e.g., floating or penetration).

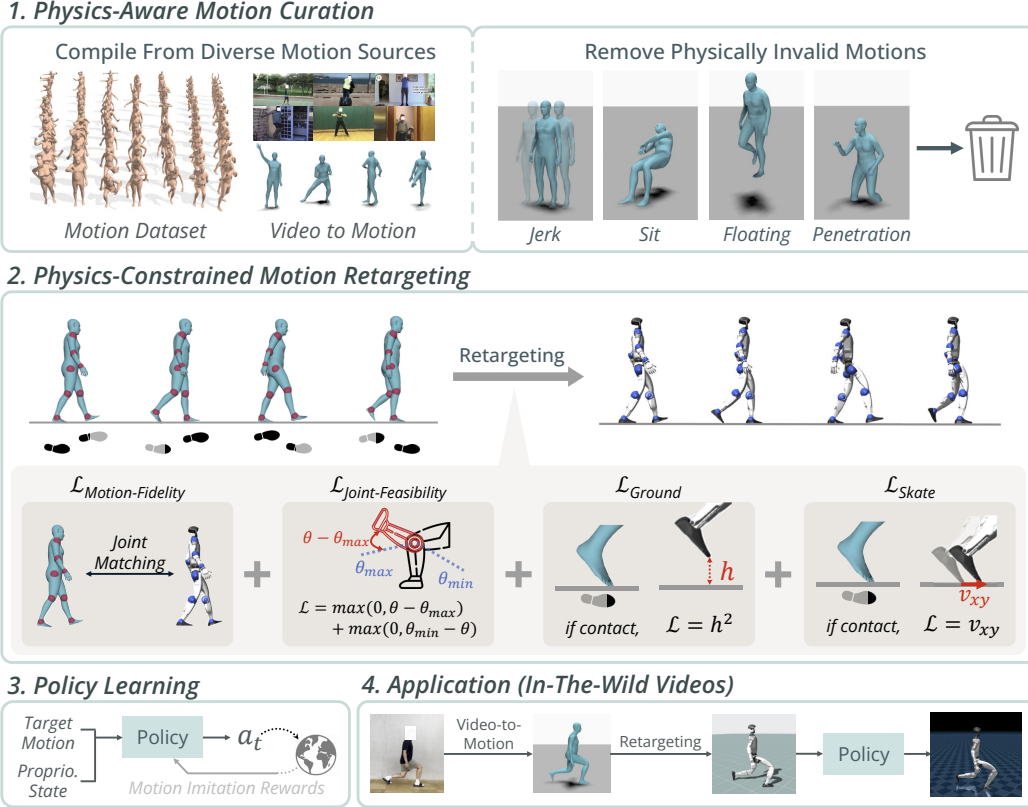


Figure 3: **Overview of the PHUMA pipeline.** Our four-stage pipeline for motion imitation learning includes: (1) Motion Curation, where we filter out problematic motions from a diverse dataset; (2) Motion Retargeting, where the filtered motions are retargeted to the humanoid using PhySINK; (3) Policy Learning, where a policy is trained to imitate the retargeted motions; and (4) Inference, where the trained policy is used to control the humanoid, enabling it to imitate motions from unseen videos processed by a video-to-motion model.

Jitter and instability. To mitigate high-frequency jitter, we apply a low-pass Butterworth filter, which smooths the motion by removing high-frequency components while preserving the overall trajectory (Appendix A.1.1). To detect physical instability, such as sitting on a non-existent chair, we compute the center-of-mass (CoM) distance from the base of support, defined as the ground area covered by the feet in contact with the floor.

Ground contact. To ensure that the feet make proper contact with the ground, a fixed ground plane is required as a reference. However, recovered motions are often defined in a camera’s coordinate frame, which has no fixed ground, causing floating and penetration. To address this, we estimate a global ground plane by majority voting over the heights of vertices on the foot meshes, selecting the height most consistent with ground contact. Using this estimate, we subtract the ground plane’s height from the z-coordinate of every joint in every frame, shifting the entire motion so that the ground plane aligns with $z = 0$ (Appendix A.1.2). We then compute a contact score for each foot region (e.g., heel, toe), measuring how close its vertices are to the ground plane in each frame.

With a reliable ground plane established, we segment all sequences into 4-second clips and discard any clip that exhibits (i) excessive jerk, indicating high-frequency jitter; (ii) a CoM position far outside its base of support, indicating physical instability; or (iii) insufficient foot-ground contact, indicating floating. By filtering at the clip level rather than the full sequence, we preserve valid segments even when parts of the original sequence are flawed (Appendix A.1.3).

Finally, we augment these curated motions with data from LaFAN1, LocoMuJoCo, and our own video captures. The resulting PHUMA dataset is a large-scale collection of 73.0 hours of physically reliable motion across 76.0K clips, with the full composition in Appendix A.2.

Table 1: **Quantitative comparison and ablation study of retargeting methods.** We evaluate performance on the G1 humanoid, showing the progressive impact of adding each of our proposed physical constraint losses. (H1-2 results in Appendix G)

	Motion Fidelity (%)	Joint Feasibility (%)	Non-Floating (%)	Non-Penetration (%)	Non-Skating (%)
IK	27.6	91.7	55.6	47.8	59.7
GMR	56.3	81.8	14.7	100.0	67.7
SINK	94.8	95.9	96.4	14.9	55.4
+ Joint Feasibility Loss	94.9	100.0	96.4	14.8	55.6
+ Grounding Loss	94.9	100.0	99.9	97.2	53.6
+ Skating Loss = PhySINK	94.8	100.0	99.9	96.8	89.7

3.2 Physics-Constrained Motion Retargeting

After curation, the next step is to retarget human motions to the humanoid embodiment. Standard inverse kinematics (**IK**) rigidly maps human joint positions to the humanoid skeleton, distorting the original motion when the two skeletons differ in proportion. Shape-adaptive inverse kinematics (**SINK**) preserves motion style by first reshaping the human body to match the humanoid’s kinematic structure, but does not account for physical plausibility, leading to artifacts such as joint violations and unrealistic ground interactions (Figure 1).

PhySINK. We propose Physically constrained Shape-adaptive Inverse Kinematics (PhySINK), which augments SINK with three physics-aware constraints. Our key insight is that physical artifacts in retargeting arise from three distinct sources: the mechanical limits of the robot, the ground plane, and contact consistency. Each can be addressed by a dedicated loss term during optimization. Specifically, PhySINK optimizes a composite objective as follows:

- **Motion Fidelity Loss** ($\mathcal{L}_{\text{Fidelity}}$) keeps the retargeted motion kinematically close to the source by minimizing per-joint position and per-link orientation errors.
- **Joint Feasibility Loss** ($\mathcal{L}_{\text{Feasibility}}$) penalizes joint angles and velocities that exceed the robot’s mechanical limits, preventing over-extension and unrealistic actuation.
- **Grounding Loss** ($\mathcal{L}_{\text{Ground}}$) aligns the foot height with the ground plane during contact frames, eliminating floating and penetration.
- **Skating Loss** ($\mathcal{L}_{\text{Skate}}$) suppresses horizontal foot velocity during contact, preventing the foot from sliding while it is in contact with the ground.

The full objective is:

$$\mathcal{L}_{\text{PhySINK}} = \mathcal{L}_{\text{Fidelity}} + w_{\text{Feasibility}}\mathcal{L}_{\text{Feasibility}} + w_{\text{Ground}}\mathcal{L}_{\text{Ground}} + w_{\text{Skate}}\mathcal{L}_{\text{Skate}} \quad (1)$$

By jointly optimizing these terms, PhySINK produces motions that faithfully reflect the human motion while remaining physically reliable. Formal definitions of each loss are provided in Appendix B.

Evaluation. We measure physical reliability across five complementary metrics, each defined as the percentage of frames satisfying a physical criterion: *Motion Fidelity* (per-joint position error < 10 cm and per-link orientation error < 10°), *Joint Feasibility* (joint positions and velocities within 98% of mechanical limits), *Non-Floating* (foot within 1 cm above ground during contact), *Non-Penetration* (foot within 1 cm below ground during contact), and *Non-Skating* (horizontal foot velocity < 10 cm/s during contact). We retarget curated motions onto the Unitree G1 and H1-2 [81, 82], comparing against a standard IK solver [83], GMR [69], and SINK.

As shown in Table 1, IK and GMR rely on linear scaling between the human and robot skeletons, which fails to account for body shape differences and loses motion fidelity. SINK recovers fidelity by adapting body shape, but suffers from physical violations. GMR achieves the highest Non-Penetration by lowering the entire motion to its lowest contact point, but this causes severe floating elsewhere. PhySINK is the only method that performs consistently well across all five metrics. Qualitative comparisons are provided in Appendix B.2.

4 Experiments

In this section, we evaluate the effectiveness of our curation and retargeting pipeline, together with the resulting PHUMA dataset, along four axes corresponding to the following research questions:

RQ1. Does physics-aware data curation improve downstream motion imitation?

RQ2. How does our proposed PhysSINK retargeting method compare with established retargeting approaches (IK, GMR, SINK) in terms of motion imitation performance?

RQ3. How effective is PHUMA as a training data for motion imitation, compared with prior humanoid motion datasets (LaFAN1, AMASS, Humanoid-X)?

RQ4. Does PHUMA’s advantage in motion tracking extend from simulation to the real robot?

4.1 Experiment Setup

Training. The motion tracking framework for in-simulation evaluation is based on MaskedMimic [8], while BeyondMimic [18] is utilized for sim-to-real transfer. In both approaches, policies are trained to imitate retargeted motions by maximizing motion tracking reward signals via PPO [84]. In-simulation experiments involve both the Unitree G1 (29 DoF) and H1-2 (21 DoF, excluding wrist joints) humanoids, whereas real-world validation is performed exclusively on the Unitree G1. Comprehensive training details, including the observation space, reward function, and PPO parameters, are provided in Appendix C.

Evaluation. Performance evaluation of the trained policies is conducted across two distinct datasets. The first comprises the PHUMA test split, containing approximately 7.5K motions (10% of PHUMA) held out during training. The second consists of 504 self-collected video sequences, which are converted into motion trajectories via a video-to-motion model; processing details are provided in Appendix D.1. To address RQ1–RQ3, the success rate [9–11, 37] is measured using a 0.15m threshold, which is stricter than the conventional 0.5m limit (see Appendix D.2). For RQ4, due to the unavailability of mocap equipment in the real-world setup—precluding the recording of global translations—the evaluation relies on local mean per-joint position error (MPJPE, mm) alongside DoF velocity (deg/frame) and acceleration (deg/frame²) errors instead of their global counterparts.

Table 2: **Imitation Performance: Effect of Physics-Aware Curation.** MaskedMimic policies trained on Humanoid-X subsets with varying curation filters, on Unitree G1. All variants use SINK retargeting to isolate filtering effect. Hours: remaining dataset size after filtering.

Variant	Hours	Curation Filter				PHUMA Test					Unseen Video				
		Jerk	FC	Height	BoS	Total	Stat.	Ang.	Vert.	Horiz.	Total	Stat.	Ang.	Vert.	Horiz.
Humanoid-X	231	✗	✗	✗	✗	50.6	78.4	43.0	26.0	31.8	39.1	78.0	39.6	23.0	6.5
+ Jerk only	141	✓	✗	✗	✗	83.0	91.5	77.6	72.3	88.5	77.6	100.0	78.8	62.8	61.5
+ FC only	123	✗	✓	✗	✗	82.9	91.3	77.8	70.4	89.1	78.2	99.1	79.3	61.7	65.9
+ Height only	136	✗	✗	✓	✗	80.6	90.7	74.6	69.3	85.1	74.0	98.3	76.4	61.7	50.5
+ BoS only	110	✗	✗	✗	✓	81.3	90.2	76.2	72.0	84.4	74.8	96.6	79.8	54.3	57.1
All filters	62	✓	✓	✓	✓	87.0	93.0	82.7	81.8	90.3	79.6	98.3	82.8	59.6	69.2

4.2 Effect of Physics-Aware Curation

To isolate the contribution of physics-aware curation, we conduct this evaluation under a controlled setup. We retarget all motions with SINK, which applies no physical correction at the retargeting stage, so that any change in downstream performance can be attributed to curation alone. LaFAN1 and LocoMuJoCo are excluded from this experiment, as they are already provided in retargeted form and would entangle retargeting effects with curation effects, and the validation split is held out throughout. As shown in Tables 2, applying any single filtering component improves motion tracking performance over the no-curation baseline, and applying all components yields a substantially larger gain, even though the fully filtered set contains roughly one quarter of the unfiltered motion volume. These results indicate that the proposed physics-aware curation contributes meaningfully to motion tracking performance, with data quality outweighing raw quantity.

4.3 PhySINK Retargeting Method Effectiveness

To evaluate PhySINK, we compare it against three established retargeting baselines (IK, GMR, and SINK) using the AMASS dataset. Since AMASS consists of clean, motion-capture data, it effectively removes the influence of data curation, allowing us to strictly isolate the retargeting performance. We retarget the identical motions with each method and train a separate full-state tracking policy for each baseline. As shown in Table 3, PhySINK consistently outperforms the baselines on both evaluation sets, demonstrating that physically reliable retargeting leads to better imitation performance. Notably, the largest gains appear on angular and vertical motions, where balance is critical and physical reliability of training data directly affects policy learning.

Table 3: **Motion tracking performance across retargeting approaches.** Success rates of policies trained on AMASS data retargeted by IK, GMR, SINK, and PhySINK, evaluated on the G1 humanoid robot using two test sets: PHUMA Test and Unseen Video. (H1-2 results in Appendix G)

Retarget	PHUMA Test					Unseen Video				
	Total	Stationary	Angular	Vertical	Horizontal	Total	Stationary	Angular	Vertical	Horizontal
IK	52.8	75.3	43.9	24.3	44.2	54.6	89.3	54.6	32.7	43.3
GMR	61.7	80.2	51.7	32.5	74.0	59.3	87.1	64.5	31.9	40.7
SINK	76.2	88.5	72.1	56.8	66.8	70.2	90.7	75.0	62.7	44.1
PhySINK	79.5	89.9	76.1	61.1	69.5	72.8	93.3	78.2	65.6	47.3

4.4 PHUMA Dataset Effectiveness

Having demonstrated PhySINK’s effectiveness, we now compare PHUMA against existing humanoid datasets. We train full-state policies on four datasets with different characteristics: LaFAN1 (small-scale, high-quality), AMASS (medium-scale, moderate-quality), Humanoid-X (large-scale, lower-quality), and PHUMA (large-scale, high-quality). For AMASS, we apply the widely-used SINK retargeting method since it provides human motion source data, while LaFAN1 and Humanoid-X are used directly as pre-existing humanoid datasets. As shown in Table 4, policies trained on PHUMA achieve the highest success rates across all motion categories and both humanoids. The results reveal that neither scale nor quality alone is sufficient: Humanoid-X, despite its large size, underperforms due to quality issues, while the cleaner LaFAN1 and AMASS lack coverage in several motion types. By combining large scale with high-quality motions, PHUMA delivers consistently superior performance across diverse behaviors.

Table 4: **Motion tracking performance across datasets.** Success rates of policies trained on LaFAN1, AMASS, Humanoid-X, and PHUMA, evaluated across motion categories on the G1 humanoid robot using two test sets: PHUMA Test and Unseen Video. (H1-2 results in Appendix G)

Dataset	Hours	PHUMA Test					Unseen Video				
		Total	Stationary	Angular	Vertical	Horizontal	Total	Stationary	Angular	Vertical	Horizontal
LaFAN1	2.4	46.1	66.1	36.2	24.0	42.5	28.4	46.9	28.4	19.6	10.5
AMASS	20.9	76.2	88.5	72.1	56.8	66.8	78.2	90.7	75.0	62.7	44.1
Humanoid-X	231.4	50.6	78.4	43.0	26.0	31.8	39.1	78.0	39.6	23.0	6.5
PHUMA	73.0	92.7	95.6	91.7	86.0	85.6	82.9	96.7	88.0	71.8	67.1

4.5 Real-World Experiment

To verify whether the advantage of PHUMA-trained policies transfers to physical hardware, we adopt BeyondMimic [18], a motion tracking framework with proven sim-to-real transfer on a real Unitree G1. Since the original BeyondMimic is designed for single-motion tracking, we extend it to multi-motion tracking by augmenting the policy’s observation space with a learned latent encoding of the future reference trajectory; full details are provided in Appendix C. We train policies on AMASS and PHUMA in IsaacSim and evaluate zero-shot tracking performance on 6 motions per category (stationary, angular, vertical, and horizontal) in the PHUMA test split.

As shown in Table 5 and Figure 4, the PHUMA-trained policy achieves lower tracking errors across all metrics and exhibits qualitatively more faithful motion tracking, indicating that PHUMA’s advantages in scale and physical reliability extend from simulation to the real robot.

Table 5: **Real-World Tracking Results.** Tracking errors of policies trained on AMASS and PHUMA, evaluated on 6 motions per category from the PHUMA test set, on the Unitree G1.

Dataset	E_{mpipe} (mm) ↓					$E_{\text{dof.vel}}$ (deg/frame) ↓					$E_{\text{dof.acc}}$ (deg/frame ²) ↓				
	Total	Stat.	Ang.	Vert.	Hor.	Total	Stat.	Ang.	Vert.	Hor.	Total	Stat.	Ang.	Vert.	Hor.
AMASS	41.0	27.3	47.5	49.9	39.4	3.20	1.81	4.10	3.14	3.77	1.50	0.77	2.09	1.33	1.80
PHUMA	34.3	23.2	40.4	42.6	31.1	2.69	1.41	3.07	2.68	3.60	1.29	0.58	1.43	1.18	1.96

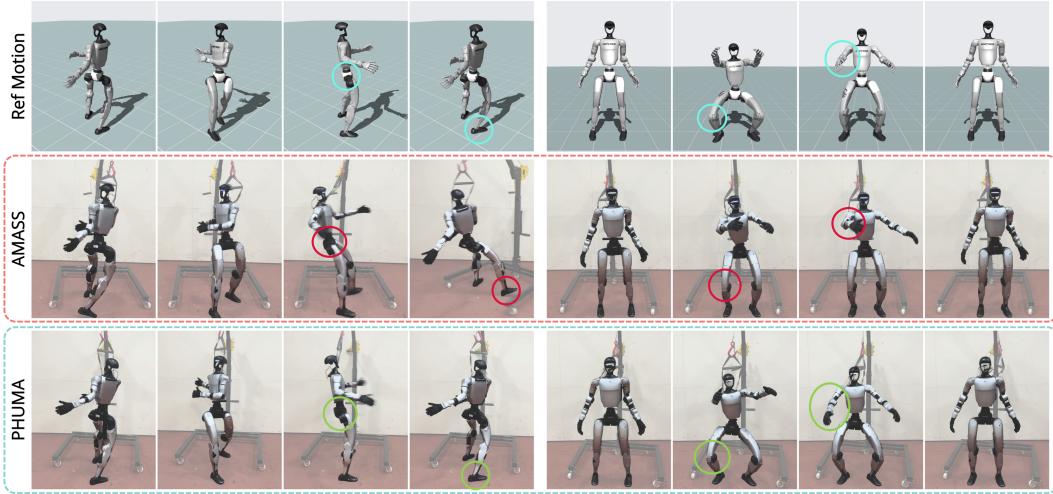


Figure 4: **Real-World Deployment.** Each row shows the reference motion (top), the motion tracked by the AMASS-trained policy (middle), and the motion tracked by the PHUMA-trained policy (bottom), demonstrating that PHUMA achieves closer alignment with the reference across all sequences.

5 Limitations

While PHUMA advances the scale and physical reliability of humanoid motion data, several directions remain open for future work. First, our pipeline focuses on flat-terrain locomotion and does not yet cover motions involving scene interaction (e.g., object manipulation, sitting, climbing) or uneven terrain; extending it to such settings would require jointly modeling humanoid dynamics with environment geometry and contact. Second, a substantial portion of motions estimated from video was filtered out during curation to ensure physical reliability, reflecting the current limitations of video-to-motion recovery; as this technology matures, future versions of PHUMA can capture a larger and more diverse range of human behaviors. Finally, while PhySINK substantially reduces physical artifacts during retargeting, the motions in PHUMA do not entirely eliminate them, and further closing this gap remains an important direction for future work.

6 Conclusion

We introduced PHUMA, a large-scale, physically reliable humanoid locomotion dataset that overcomes the limitations of existing motion imitation pipelines. Unlike prior video-driven datasets prone to artifacts such as floating, ground penetration, and joint violations, PHUMA combines diverse human videos with physics-aware curation and PhySINK, our physics-constrained retargeting method, to produce motions that are both diverse and physically reliable. On the Unitree G1 and H1-2 humanoids, policies trained on PHUMA consistently outperform those trained on LaFAN1, AMASS, and Humanoid-X, with ablations confirming that both curation and PhySINK contribute meaningfully. These advantages further extend to a real Unitree G1, where PHUMA-trained policies achieve lower tracking errors than AMASS-trained counterparts. Together, these results show that advancing humanoid motion tracking depends not just on having more data, but on having physically reliable data. PHUMA achieves both: it scales up data by incorporating diverse human videos, while ensuring physical reliability through careful curation and retargeting.

References

- [1] J. Mao, S. Zhao, S. Song, T. Shi, J. Ye, M. Zhang, H. Geng, J. Malik, V. C. Guizilini, and Y. Wang. Universal humanoid robot pose learning from internet human videos. In *ICRA 2025 Workshop: Human-Centered Robot Learning in the Era of Big Data and Large Models*, 2025. URL <https://openreview.net/forum?id=2pBjMDj6uJ>.
- [2] J. Hwangbo, J. Lee, A. Dosovitskiy, D. Bellicoso, V. Tsounis, V. Koltun, and M. Hutter. Learning agile and dynamic motor skills for legged robots. *Science Robotics*, 4(26):eaau5872, 2019.
- [3] J. Lee, J. Hwangbo, L. Wellhausen, V. Koltun, and M. Hutter. Learning quadrupedal locomotion over challenging terrain. *Science robotics*, 5(47):eabc5986, 2020.
- [4] J. Tan, T. Zhang, E. Coumans, A. Iscen, Y. Bai, D. Hafner, S. Bohez, and V. Vanhoucke. Sim-to-real: Learning agile locomotion for quadruped robots. *arXiv preprint arXiv:1804.10332*, 2018.
- [5] N. Hansen, H. Su, and X. Wang. Td-mpc2: Scalable, robust world models for continuous control. In *International Conference on Learning Representations (ICLR)*, 2024.
- [6] C. Sferrazza, D.-M. Huang, X. Lin, Y. Lee, and P. Abbeel. Humanoidbench: Simulated humanoid benchmark for whole-body locomotion and manipulation. *Robotics: Science and Systems 2024*, 2024.
- [7] X. B. Peng, P. Abbeel, S. Levine, and M. Van de Panne. Deepmimic: Example-guided deep reinforcement learning of physics-based character skills. *ACM Transactions On Graphics (TOG)*, 37(4):1–14, 2018.
- [8] C. Tessler, Y. Guo, O. Nabati, G. Chechik, and X. B. Peng. Maskedmimic: Unified physics-based character control through masked motion inpainting. *ACM Transactions on Graphics (TOG)*, 43(6):1–21, 2024.
- [9] T. He, Z. Luo, W. Xiao, C. Zhang, K. Kitani, C. Liu, and G. Shi. Learning human-to-humanoid real-time whole-body teleoperation. In *2024 IEEE/RSJ International Conference on Intelligent Robots and Systems (IROS)*, pages 8944–8951. IEEE, 2024.
- [10] W. Xie, J. Han, J. Zheng, H. Li, X. Liu, J. Shi, W. Zhang, C. Bai, and X. Li. Kungfubot: Physics-based humanoid whole-body control for learning highly-dynamic skills. In *The Thirtieth Annual Conference on Neural Information Processing Systems*, 2025. URL <https://openreview.net/forum?id=LCPoXt0pzm>.
- [11] T. He, J. Gao, W. Xiao, Y. Zhang, Z. Wang, J. Wang, Z. Luo, G. He, N. Sobanbabu, C. Pan, Z. Yi, G. Qu, K. Kitani, J. Hodgins, L. J. Fan, Y. Zhu, C. Liu, and G. Shi. Asap: Aligning simulation and real-world physics for learning agile humanoid whole-body skills. In *Robotics: Science and Systems (RSS)*, June 2025.
- [12] F. G. Harvey, M. Yurick, D. Nowrouzezahrai, and C. Pal. Robust motion in-betweening. *ACM Transactions on Graphics (TOG)*, 39(4):60–1, 2020.
- [13] N. Mahmood, N. Ghorbani, N. F. Troje, G. Pons-Moll, and M. J. Black. Amass: Archive of motion capture as surface shapes. In *Proceedings of the IEEE/CVF international conference on computer vision*, pages 5442–5451, 2019.
- [14] M. Loper, N. Mahmood, J. Romero, G. Pons-Moll, and M. J. Black. Smpl: A skinned multi-person linear model. In *Seminal Graphics Papers: Pushing the Boundaries, Volume 2*, pages 851–866. 2023.
- [15] G. Pavlakos, V. Choutas, N. Ghorbani, T. Bolkart, A. A. Osman, D. Tzionas, and M. J. Black. Expressive body capture: 3d hands, face, and body from a single image. In *Proceedings of the IEEE/CVF conference on computer vision and pattern recognition*, pages 10975–10985, 2019.

- [16] M. Kocabas, N. Athanasiou, and M. J. Black. Vibe: Video inference for human body pose and shape estimation. In *Proceedings of the IEEE/CVF conference on computer vision and pattern recognition*, pages 5253–5263, 2020.
- [17] T. He, Z. Luo, X. He, W. Xiao, C. Zhang, W. Zhang, K. M. Kitani, C. Liu, and G. Shi. Omnih2o: Universal and dexterous human-to-humanoid whole-body teleoperation and learning. In *8th Annual Conference on Robot Learning*, 2024. URL <https://openreview.net/forum?id=oL1WEZQa18>.
- [18] T. E. Truong, Q. Liao, X. Huang, G. Tevet, C. K. Liu, and K. Sreenath. Beyondmimic: From motion tracking to versatile humanoid control via guided diffusion. *arXiv preprint arXiv:2508.08241*, 2025.
- [19] Carnegie mellon university graphics lab motion capture database. <http://mocap.cs.cmu.edu>, 2003. The data was captured with funding from NSF EIA-0196217. Acknowledgment of the database is appreciated in any published work.
- [20] S. Zhang, Q. Ma, Y. Zhang, Z. Qian, T. Kwon, M. Pollefeys, F. Bogo, and S. Tang. Egobody: Human body shape and motion of interacting people from head-mounted devices. In *European conference on computer vision*, pages 180–200. Springer, 2022.
- [21] F. Al-Hafez, G. Zhao, J. Peters, and D. Tateo. Locomujoco: A comprehensive imitation learning benchmark for locomotion. In *6th Robot Learning Workshop, NeurIPS*, 2023.
- [22] Bones Studio. BONES-SEED: Skeletal everyday embodied dataset. <https://bones.studio/datasets/seed>, 2026.
- [23] S. Shin, J. Kim, E. Halilaj, and M. J. Black. Wham: Reconstructing world-grounded humans with accurate 3d motion. In *Proceedings of the IEEE/CVF Conference on Computer Vision and Pattern Recognition*, pages 2070–2080, 2024.
- [24] Y. Wang, Z. Wang, L. Liu, and K. Daniilidis. Tram: Global trajectory and motion of 3d humans from in-the-wild videos. In *European Conference on Computer Vision*, pages 467–487. Springer, 2024.
- [25] Z. Shen, H. Pi, Y. Xia, Z. Cen, S. Peng, Z. Hu, H. Bao, R. Hu, and X. Zhou. World-grounded human motion recovery via gravity-view coordinates. In *SIGGRAPH Asia 2024 Conference Papers*, pages 1–11, 2024.
- [26] Z. Gu, J. Li, W. Shen, W. Yu, Z. Xie, S. McCrory, X. Cheng, A. Shamsah, R. Griffin, C. K. Liu, et al. Humanoid locomotion and manipulation: Current progress and challenges in control, planning, and learning. *arXiv preprint arXiv:2501.02116*, 2025.
- [27] J. Lin, A. Zeng, S. Lu, Y. Cai, R. Zhang, H. Wang, and L. Zhang. Motion-x: A large-scale 3d expressive whole-body human motion dataset. *Advances in Neural Information Processing Systems*, 36:25268–25280, 2023.
- [28] Y. Zhang, J. Lin, A. Zeng, G. Wu, S. Lu, Y. Fu, Y. Cai, R. Zhang, H. Wang, and L. Zhang. Motion-x++: A large-scale multimodal 3d whole-body human motion dataset. *arXiv preprint arXiv:2501.05098*, 2025.
- [29] J. Chung, C.-h. Wu, H.-r. Yang, Y.-W. Tai, and C.-K. Tang. Haa500: Human-centric atomic action dataset with curated videos. In *Proceedings of the IEEE/CVF international conference on computer vision*, pages 13465–13474, 2021.
- [30] Z. Cai, D. Ren, A. Zeng, Z. Lin, T. Yu, W. Wang, X. Fan, Y. Gao, Y. Yu, L. Pan, et al. Humman: Multi-modal 4d human dataset for versatile sensing and modeling. In *European Conference on Computer Vision*, pages 557–577. Springer, 2022.

- [31] S. Tsuchida, S. Fukayama, M. Hamasaki, and M. Goto. Aist dance video database: Multi-genre, multi-dancer, and multi-camera database for dance information processing. In *ISMIR*, volume 1, page 6, 2019.
- [32] K. Fan, S. Lu, M. Dai, R. Yu, L. Xiao, Z. Dou, J. Dong, L. Ma, and J. Wang. Go to zero: Towards zero-shot motion generation with million-scale data. In *Proceedings of the IEEE/CVF International Conference on Computer Vision*, pages 13336–13348, 2025.
- [33] J. Ni, Z. Wang, W. Lin, A. Bar, Y. LeCun, T. Darrell, J. Malik, and R. Herzig. From generated human videos to physically plausible robot trajectories. *arXiv preprint arXiv:2512.05094*, 2025.
- [34] Y. Wei, Z. Wang, K. Yin, Y. Hu, J. Wang, and S. Chen. Unveiling the impact of data and model scaling on high-level control for humanoid robots. *arXiv preprint arXiv:2511.09241*, 2025.
- [35] Y. Wang, Q. Zhao, Y. F. Lau, R. Yu, H. W. Tsui, Q. Chen, J. Wang, J. Pang, and P. Tan. Humanx: Toward agile and generalizable humanoid interaction skills from human videos. *arXiv preprint arXiv:2602.02473*, 2026.
- [36] H. Weng, Y. Li, N. Sobanbabu, Z. Wang, Z. Luo, T. He, D. Ramanan, and G. Shi. Hdmi: Learning interactive humanoid whole-body control from human videos. *arXiv preprint arXiv:2509.16757*, 2025.
- [37] Z. Luo, J. Cao, A. W. Winkler, K. Kitani, and W. Xu. Perpetual humanoid control for real-time simulated avatars. In *International Conference on Computer Vision (ICCV)*, 2023.
- [38] Z. Luo, J. Cao, J. Merel, A. Winkler, J. Huang, K. M. Kitani, and W. Xu. Universal humanoid motion representations for physics-based control. In *The Twelfth International Conference on Learning Representations*, 2024. URL <https://openreview.net/forum?id=0r0d8Px002>.
- [39] S. Goel, G. Pavlakos, J. Rajasegaran, A. Kanazawa, and J. Malik. Humans in 4d: Reconstructing and tracking humans with transformers. In *Proceedings of the IEEE/CVF International Conference on Computer Vision*, pages 14783–14794, 2023.
- [40] V. Ye, G. Pavlakos, J. Malik, and A. Kanazawa. Decoupling human and camera motion from videos in the wild. In *Proceedings of the IEEE/CVF conference on computer vision and pattern recognition*, pages 21222–21232, 2023.
- [41] R. Yu, H. Park, and J. Lee. Human dynamics from monocular video with dynamic camera movements. *ACM Transactions on Graphics (TOG)*, 40(6):1–14, 2021.
- [42] N. Ugrinovic, B. Pan, G. Pavlakos, D. Paschalidou, B. Shen, J. Sanchez-Riera, F. Moreno-Noguer, and L. Guibas. Multiphys: Multi-person physics-aware 3d motion estimation. In *Proceedings of the IEEE/CVF Conference on Computer Vision and Pattern Recognition*, pages 2331–2340, 2024.
- [43] N. Wagener, A. Kolobov, F. Vieira Frujeri, R. Loynd, C.-A. Cheng, and M. Hausknecht. Mocapact: A multi-task dataset for simulated humanoid control. *Advances in Neural Information Processing Systems*, 35:35418–35431, 2022.
- [44] Z. Luo, R. Hachiuma, Y. Yuan, and K. Kitani. Dynamics-regulated kinematic policy for egocentric pose estimation. *Advances in Neural Information Processing Systems*, 34:25019–25032, 2021.
- [45] N. Hansen, J. S. V, V. Sobal, Y. LeCun, X. Wang, and H. Su. Hierarchical world models as visual whole-body humanoid controllers. In *The Thirteenth International Conference on Learning Representations*, 2025. URL <https://openreview.net/forum?id=7wuJMvK639>.

- [46] A. Tirinzoni, A. Touati, J. Farebrother, M. Guzek, A. Kanervisto, Y. Xu, A. Lazaric, and M. Pirodda. Zero-shot whole-body humanoid control via behavioral foundation models. In *The Thirteenth International Conference on Learning Representations*, 2025. URL <https://openreview.net/forum?id=9s0R0nYltz>.
- [47] Z. Zhang, S. Bashkirov, D. Yang, Y. Shi, M. Taylor, and X. B. Peng. Physics-based motion imitation with adversarial differential discriminators. In *Proceedings of the SIGGRAPH Asia 2025 Conference Papers*, pages 1–12, 2025.
- [48] J. Zhang, H. Liang, R. Zhang, B. Li, J. Zhang, X. Chen, J. Wang, L. Xu, and J. Yu. Script: Scalable diffusion policy with multi-stage training for language-driven physics-based humanoid control. *arXiv preprint arXiv:2605.22894*, 2026.
- [49] I. Radosavovic, S. Kamat, T. Darrell, and J. Malik. Learning humanoid locomotion over challenging terrain. *arXiv preprint arXiv:2410.03654*, 2024.
- [50] Z. Fu, Q. Zhao, Q. Wu, G. Wetzstein, and C. Finn. Humanplus: Humanoid shadowing and imitation from humans. In *Conference on Robot Learning (CoRL)*, 2024.
- [51] X. Cheng, Y. Ji, J. Chen, R. Yang, G. Yang, and X. Wang. Expressive whole-body control for humanoid robots. *Robotics: Science and Systems 2024*, 2024.
- [52] M. Ji, X. Peng, F. Liu, J. Li, G. Yang, X. Cheng, and X. Wang. Exbody2: Advanced expressive humanoid whole-body control. *arXiv preprint arXiv:2412.13196*, 2024.
- [53] Z. Chen, M. Ji, X. Cheng, X. Peng, X. B. Peng, and X. Wang. Gmt: General motion tracking for humanoid whole-body control. *arXiv preprint arXiv:2506.14770*, 2025.
- [54] Y. Li, Y. Lin, J. Cui, T. Liu, W. Liang, Y. Zhu, and S. Huang. Clone: Closed-loop whole-body humanoid teleoperation for long-horizon tasks. *arXiv preprint arXiv:2506.08931*, 2025.
- [55] Z. Luo, Y. Yuan, T. Wang, C. Li, S. Chen, F. Castaneda, Z.-A. Cao, J. Li, D. Minor, Q. Ben, et al. Sonic: Supersizing motion tracking for natural humanoid whole-body control. *arXiv preprint arXiv:2511.07820*, 2025.
- [56] Y. Li, P. Zhi, Y. Wang, T. Liu, S. Yan, W. Liu, X. Wang, B. Jia, and S. Huang. Omnitrack: General motion tracking via physics-consistent reference. *arXiv preprint arXiv:2602.23832*, 2026.
- [57] J. Li, X. Cheng, T. Huang, S. Yang, R.-Z. Qiu, and X. Wang. Amo: Adaptive motion optimization for hyper-dexterous humanoid whole-body control. *Robotics: Science and Systems 2025*, 2025.
- [58] Y. Wang, S. Zhu, P. Zhi, Y. Li, J. Li, Y.-L. Li, Y. Xiao, X. Wang, B. Jia, and S. Huang. Omnixtreme: Breaking the generality barrier in high-dynamic humanoid control. *arXiv preprint arXiv:2602.23843*, 2026.
- [59] D. Rempe, M. Petrovich, Y. Yuan, H. Zhang, X. B. Peng, Y. Jiang, T. Wang, U. Iqbal, D. Minor, M. de Ruyter, et al. Kimodo: Scaling controllable human motion generation. *arXiv preprint arXiv:2603.15546*, 2026.
- [60] S. Zhao, Y. Ze, Y. Wang, C. K. Liu, P. Abbeel, G. Shi, and R. Duan. Resmimic: From general motion tracking to humanoid whole-body loco-manipulation via residual learning. *arXiv preprint arXiv:2510.05070*, 2025.
- [61] S. Yin, Y. Ze, H.-X. Yu, C. K. Liu, and J. Wu. Visualmimic: Visual humanoid loco-manipulation via motion tracking and generation. *arXiv preprint arXiv:2509.20322*, 2025.
- [62] M. Gleicher. Retargetting motion to new characters. In *Proceedings of the 25th annual conference on Computer graphics and interactive techniques*, pages 33–42, 1998.

- [63] C. M. Kim, B. Yi, H. Choi, Y. Ma, K. Goldberg, and A. Kanazawa. Pyroki: A modular toolkit for robot kinematic optimization. In *2025 IEEE/RSJ International Conference on Intelligent Robots and Systems (IROS)*, 2025. URL <https://arxiv.org/abs/2505.03728>.
- [64] E. S. Ho, T. Komura, and C.-L. Tai. Spatial relationship preserving character motion adaptation. In *ACM SIGGRAPH 2010 papers*, pages 1–8. 2010.
- [65] J. Zhang, J. Weng, D. Kang, F. Zhao, S. Huang, X. Zhe, L. Bao, Y. Shan, J. Wang, and Z. Tu. Skinned motion retargeting with residual perception of motion semantics & geometry. In *Proceedings of the IEEE/CVF Conference on Computer Vision and Pattern Recognition*, pages 13864–13872, 2023.
- [66] I. Radosavovic, B. Zhang, B. Shi, J. Rajasegaran, S. Kamat, T. Darrell, K. Sreenath, and J. Malik. Humanoid locomotion as next token prediction. *Advances in neural information processing systems*, 37:79307–79324, 2024.
- [67] S. Caron, Y. De Mont-Marin, R. Budhiraja, S. H. Bang, I. Domrachev, S. Nedelchev, peterd NV, and J. Vaillant. Pink: Python inverse kinematics based on Pinocchio, 2025. URL <https://github.com/stephane-caron/pink>.
- [68] Y. Ze, Z. Chen, J. P. Araujo, Z. ang Cao, X. B. Peng, J. Wu, and K. Liu. TWIST: Teleoperated whole-body imitation system. In *9th Annual Conference on Robot Learning*, 2025. URL <https://openreview.net/forum?id=htgNQHa6Ta>.
- [69] J. P. Araujo, Y. Ze, P. Xu, J. Wu, and C. K. Liu. Retargeting matters: General motion retargeting for humanoid motion tracking. *arXiv preprint arXiv:2510.02252*, 2025.
- [70] T. He, W. Xiao, T. Lin, Z. Luo, Z. Xu, Z. Jiang, J. Kautz, C. Liu, G. Shi, X. Wang, et al. Hover: Versatile neural whole-body controller for humanoid robots. In *2025 IEEE International Conference on Robotics and Automation (ICRA)*, pages 9989–9996. IEEE, 2025.
- [71] T. Cheynel, T. Rossi, B. Bellot-Gurlet, D. Rohmer, and M.-P. Cani. Sparse motion semantics for contact-aware retargeting. In *ACM SIGGRAPH Conference on Motion, Interaction and Games (MIG)*, 2023.
- [72] A. Allshire, H. Choi, J. Zhang, D. McAllister, A. Zhang, C. M. Kim, T. Darrell, P. Abbeel, J. Malik, and A. Kanazawa. Visual imitation enables contextual humanoid control. In *Proceedings of The Conference on Robot Learning*, Proceedings of Machine Learning Research, 2025.
- [73] Z. Chen, H. Zhang, D. Wang, J. Yu, H. Xu, Y. Wang, and R. Xiong. A whole-body motion imitation framework from human data for full-size humanoid robot. In *2025 IEEE International Conference on Real-time Computing and Robotics (RCAR)*, pages 558–563. IEEE, 2025.
- [74] L. Yang, X. Huang, Z. Wu, A. Kanazawa, P. Abbeel, C. Sferrazza, C. K. Liu, R. Duan, and G. Shi. Omniretarget: Interaction-preserving data generation for humanoid whole-body locomanipulation and scene interaction. *arXiv preprint arXiv:2509.26633*, 2025.
- [75] C. Pan, C. Wang, H. Qi, Z. Liu, H. Bharadhwaj, A. Sharma, T. Wu, G. Shi, J. Malik, and F. Hogan. Spider: Scalable physics-informed dexterous retargeting. *arXiv preprint arXiv:2511.09484*, 2025.
- [76] X. Zhang, S. Haener, V. Madabushi, and M. Tucker. Kinodynamic motion retargeting for humanoid locomotion via multi-contact whole-body trajectory optimization. *arXiv preprint arXiv:2603.09956*, 2026.
- [77] H. Wang, Q. Liao, B. Zhang, K. Ren, K. Sreenath, and X. Xiong. Spark: Skeleton-parameter aligned retargeting on humanoid robots with kinodynamic trajectory optimization. *arXiv preprint arXiv:2603.11480*, 2026.

- [78] D. Müller, A. Serifi, S. Christen, R. Grandia, E. Knoop, and M. Bächer. Reactor: Reinforcement learning for physics-aware motion retargeting. *arXiv preprint arXiv:2605.06593*, 2026.
- [79] X. Chen, H. Wu, S. Wu, M. Zhou, D. Xiang, and H. Zhang. Implicit kinodynamic motion retargeting for human-to-humanoid imitation learning. *arXiv preprint arXiv:2509.15443*, 2025.
- [80] Q. Zhao, K. Yang, X. Wang, S. Zhao, Y. Lu, X. Zhang, Q. Shen, X.-X. Long, and X. Cao. Make tracking easy: Neural motion retargeting for humanoid whole-body control. *arXiv preprint arXiv:2603.22201*, 2026.
- [81] Unitree Robotics. Unitree g1 humanoid robot. <https://www.unitree.com/g1>, 2025. Accessed: 2025-09-25.
- [82] Unitree Robotics. Unitree h1-2 humanoid robot. <https://www.unitree.com/h1>, 2025. Accessed: 2025-09-25.
- [83] K. Zakka. Mink: Python inverse kinematics based on MuJoCo, May 2025. URL <https://github.com/kevinzakka/mink>.
- [84] J. Schulman, F. Wolski, P. Dhariwal, A. Radford, and O. Klimov. Proximal policy optimization algorithms. *arXiv preprint arXiv:1707.06347*, 2017.
- [85] O. Taheri, N. Ghorbani, M. J. Black, and D. Tzionas. Grab: A dataset of whole-body human grasping of objects. In *European conference on computer vision*, pages 581–600. Springer, 2020.
- [86] J. Han, W. Xie, J. Zheng, J. Shi, W. Zhang, T. Xiao, and C. Bai. Kungfubot2: Learning versatile motion skills for humanoid whole-body control. *arXiv preprint arXiv:2509.16638*, 2025.

Appendix

A PHUMA Dataset	16
A.1 Data Preprocessing	16
A.2 Dataset Composition and Statistics	18
B Motion Retargeting	18
B.1 PhySINK Retargeting Loss	19
B.2 Comparison of Retargeting Methods	21
C Motion Imitation Learning	23
C.1 Observation Space Compositions	23
C.2 Reward Function	24
C.3 PPO Hyperparameters	25
C.4 Domain Randomization	25
D Experiment Details	27
D.1 Self-Collected Video Dataset	27
D.2 Success Rate Threshold Analysis	28
D.3 Cross-Simulator Generalization Analysis	29
E Ablation Studies	29
E.1 Mocap only and Video only data performance	29
E.2 Physics-based Filtering	30
E.3 Impact of Motion Retargeting Quality on Policy Performance	31
F Pelvis-Only Path Following Control Performance	32
G Results on H1-2 Robot	32
G.1 PhySINK Ablation on H1-2	32
G.2 Retargeting Method Comparison on H1-2	33
G.3 Dataset Effectiveness on H1-2	33

A PHUMA Dataset

A.1 Data Preprocessing

Before applying the retargeting procedure, it is essential to ensure that the human motion data is clean and robust, as this data serves as the target for the humanoid robot to follow. Raw motion data often contains noise from sensor errors, tracking inaccuracies, or estimation artifacts that can negatively impact retargeting. To address this, we apply the following preprocessing to filter and clean the motion data.

A.1.1 Low-Pass Noise Filtering for Motion Data

All motion sequences were resampled to 30 Hz. We smooth all motion channels with a zero-phase, 4th-order Butterworth low-pass filter. For root translation the cutoff is 3 Hz; for global orientation and body pose it is 6 Hz.

A.1.2 Extracting Ground Contact Information

To identify foot contact, we need foot indices from human motion source. Therefore, we identify a subset of SMPL-X foot vertices that are most indicative of ground interaction. Specifically, we select the 22 vertically lowest vertices from each foot region (left heel, left toe, right heel, right toe) in the SMPL-X default pose, totaling 88 vertices. These vertices are illustrated in Figure 5. The vertex indices corresponding to these ground-contact points are provided in Table 6.

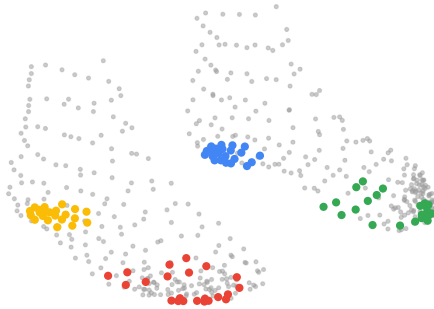


Figure 5: **SMPL-X Foot Vertices for Ground-Contact Detection.** This figure illustrates the selected foot vertices on the SMPL-X model used to detect ground contact. Blue and green points denote the left heel and left toe, while yellow and red represent the right heel and right toe, respectively. The remaining foot vertices are shown in light-gray. The clusters of colored points correspond to the specific parts of the foot that are used to check for contact with the ground, making the process more accurate and robust than using a single point.

Table 6: **SMPL-X foot vertex indices used for ground–contact detection.**

Region	Vertex indices
Left heel	8888, 8889, 8891, 8909, 8910, 8911, 8913, 8914, 8915, 8916, 8917, 8918, 8919, 8920, 8921, 8922, 8923, 8924, 8925, 8929, 8930, 8934
Left toe	5773, 5781, 5782, 5791, 5793, 5805, 5808, 5816, 5817, 5830, 5831, 5859, 5860, 5906, 5907, 5908, 5909, 5912, 5914, 5915, 5916, 5917
Right heel	8676, 8677, 8679, 8697, 8698, 8699, 8701, 8702, 8703, 8704, 8705, 8706, 8707, 8708, 8709, 8710, 8711, 8712, 8713, 8714, 8715, 8716
Right toe	8467, 8475, 8476, 8485, 8487, 8499, 8502, 8510, 8511, 8524, 8525, 8553, 8554, 8600, 8601, 8602, 8603, 8606, 8608, 8609, 8610, 8611

To correctly place a motion, it is necessary to establish a single, consistent ground plane. Simple heuristics often fail: defining the ground by the lowest foot position in the sequence can cause floating, while per-frame adjustment introduces jitter and breaks down for motions where both feet leave

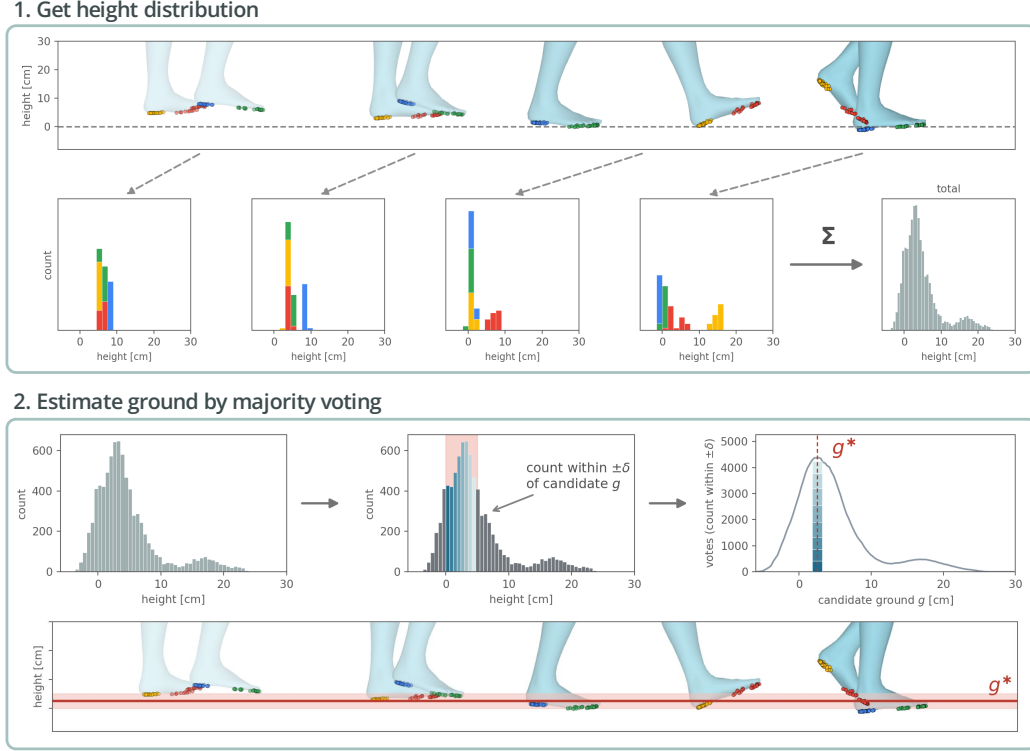


Figure 6: **Procedure of Majority-Vote Ground Estimation.** (1) shows how the foot-height distribution is obtained across all frames of a single human motion trajectory, and (2) shows how the ground height is selected from this distribution by majority vote.

the ground, such as jumping or running. Our method instead uses a majority vote to find the ground height that maximizes the duration of foot contact. Specifically, we first collect the heights of the foot vertices (Figure 5) across all frames (Figure 6.1). Because the estimated root translation of SMPL-X is noisy, we then select the optimal ground height g^* as the one with the most foot vertices falling within the band $(g - \delta, g + \delta)$ with $\delta = 2.5\text{cm}$ (Figure 6.2):

$$g^* = \arg \max_g \sum_{f=1}^F \sum_{v \in \mathcal{V}} \mathbf{1}[|h_v^f - g| < \delta], \quad (2)$$

where \mathcal{V} is the set of foot vertices, h_v^f denotes the height of vertex v at frame f , and $\mathbf{1}[\cdot]$ is the indicator function. Finally, the entire motion is shifted so that this ground sits at height zero.

A.1.3 Filtering Motion Data by Physical Information

To remove noisy data that cannot be corrected during retargeting, we evaluate each human motion clip using the following metrics: root jerk, foot contact score, pelvis height, and pelvis/spine-1 distance to the base of support (Table 7). Sub-clips that fail to meet these thresholds are discarded.

Root jerk represents rapid changes in root acceleration, indicative of abrupt or unnatural motions. High root jerk segments are excluded to ensure smooth and physically plausible trajectories.

Foot contact score measures the consistency and sufficiency of foot-ground interactions based on graded ground-contact signals defined by vertex proximity to the ground. Specifically, given a sub-clip with T frames, the foot contact score is computed as:

$$\text{Foot contact score} = \frac{1}{T} \sum_{t=1}^T \max(c_t^{LH}, c_t^{LT}, c_t^{RH}, c_t^{RT}), \quad (3)$$

Table 7: **Physics-aware data filtering metrics and thresholds.**

Metric	Threshold
Root jerk	$< 50 \text{ m/s}^3$
Foot contact score	> 0.6
Minimum pelvis height	$> 0.6 \text{ m}$
Maximum pelvis height	$< 1.5 \text{ m}$
Pelvis distance to base of support	$< 6 \text{ cm}$
Spine1 distance to base of support	$< 11 \text{ cm}$

where c_t^{LH} , c_t^{LT} , c_t^{RH} , and c_t^{RT} represent the graded ground-contact ratio at frame t for the left heel, left toe, right heel, and right toe, respectively; Figure 7 illustrates the ground-contact ratio in detail. A low foot contact score indicates significant penetration or floating, both of which are undesirable artifacts. Note that motions involving airborne phases, such as jumps, can easily satisfy this criterion as long as contact before and after the airborne phase is consistent.

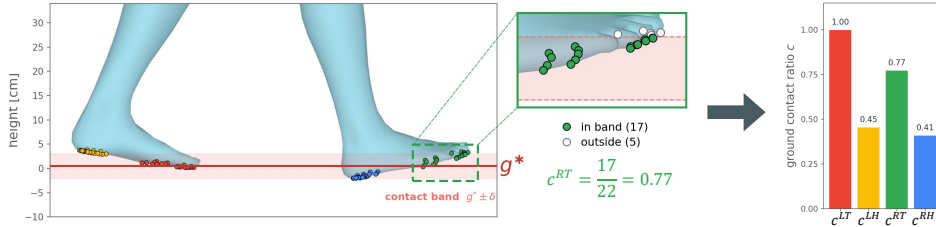


Figure 7: **Examples of Calculating the Ground-Contact Ratio.** This figure illustrates how the ground-contact ratio is computed, which is used in the foot-contact score for physics-aware curation and in the ground and skating losses for PhysSINK.

Pelvis height criteria exclude segments where the humanoid is unnaturally positioned. Specifically, the minimum height criterion filters out motions that involve the humanoid being excessively crouched or lying on the ground, while the maximum height criterion eliminates segments exhibiting unnatural floating.

Distance to the base of support criteria ensure stable and physically plausible balance. Since the SMPL-X model’s center of mass typically lies between the pelvis and spine1 joints, deviations of these joints’ horizontal-plane projections from the base of support indicate imbalance or instability infeasible for humanoids. The base of support is defined as the convex hull formed by the horizontal-plane projections of the left foot, right foot, left ankle, and right ankle joints.

A.2 Dataset Composition and Statistics

This section presents the detailed motion statistics of PHUMA. Because we collect motion data from diverse sources, ranging from MoCap to video, PHUMA achieves a well-balanced motion distribution that is not dominated by any single motion type. As shown in Figure 8b, PHUMA exhibits substantially more balanced motion coverage than existing datasets. LaFAN1 and AMASS show uneven distributions: some motion categories are entirely absent (e.g., reach, bend, and squat), while others dominate (e.g., reach, turn, and walk). In contrast, PHUMA provides balanced coverage across all categories, with substantially more examples per motion type. The detailed composition of PHUMA is given in Table 8.

B Motion Retargeting

As shown in Equation 1, the PhysSINK retargeting loss comprises four terms: motion fidelity, joint feasibility, ground, and skating losses.

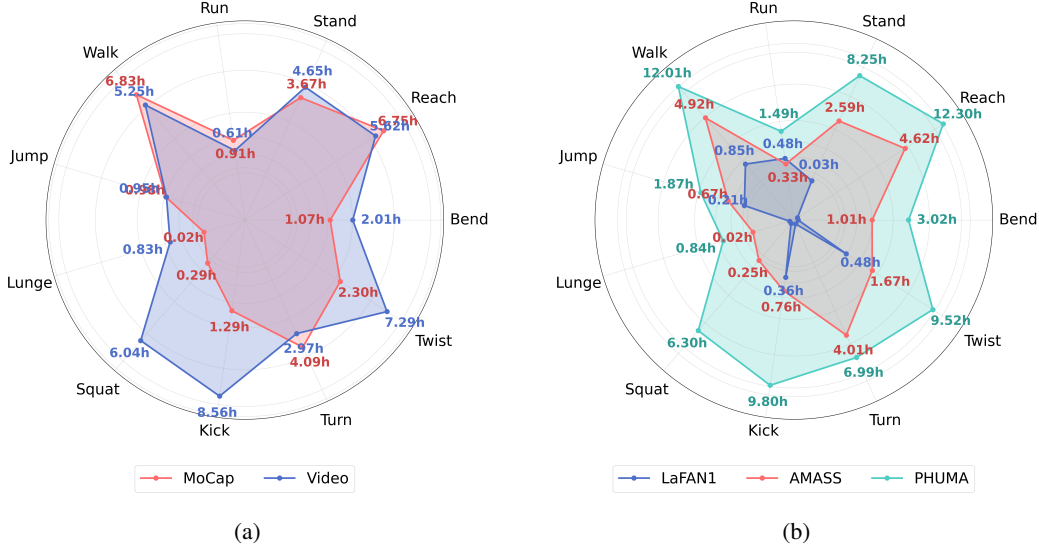


Figure 8: **Comparison of Motion Distributions.** (a) Comparison between MoCap and Video sources in PHUMA. (b) Comparison with other existing datasets.

Table 8: **Composition of the PHUMA dataset.** A summary of the number of clips and duration for each sub-dataset, categorized by source and scene. PHUMA aggregates these diverse sub-datasets, resulting in 73.0 hours of physically reliable motion clips.

Dataset	# Clip	# Frame	Duration	Source	Scene
LocoMuJoCo [21]	0.78K	0.93M	0.86h	Motion Capture	Indoor
GRAB [85]	1.73K	0.20M	1.88h	Motion Capture	Indoor
EgoBody [20]	2.12K	0.24M	2.19h	Motion Capture	Indoor
LAFAN1 [12]	2.18K	0.26M	2.40h	Motion Capture	Indoor
AMASS [13]	21.73K	2.25M	20.86h	Motion Capture	Indoor
HAA500 [29]	1.76K	0.11M	1.01h	Human Video	Outdoor
Motion-X Video [27]	33.04K	3.45M	31.98h	Human Video	Outdoor
HuMMan [30]	0.50K	0.05M	0.47h	Human Video	Indoor
AIST [31]	1.75K	0.18M	1.66h	Human Video	Indoor
IDEA400 [27]	9.94K	0.98M	9.10h	Human Video	Indoor
PHUMA Video	0.50K	0.06M	0.56h	Human Video	Outdoor
PHUMA	76.01K	7.88M	72.96h		

B.1 PhysSINK Retargeting Loss

B.1.1 Motion Fidelity Loss

The motion fidelity loss $\mathcal{L}_{\text{Fidelity}}$ encourages the retargeted humanoid motion to closely match the input SMPL-X motion. It consists of three terms:

Global Position Matching. We minimize the L1 distance between the global 3D joint positions of the SMPL-X body and the humanoid across all joints i and frames t :

$$\mathcal{L}_{\text{global-match}} = \sum_t \sum_i \|p_i^{\text{SMPL-X}}(t) - p_i^{\text{Humanoid}}(t)\|_1 \quad (4)$$

Local Joint Matching. We additionally enforce consistency of relative joint configurations (both position and orientation) between adjacent joints. Let m_{ij} be a binary adjacency mask (1 if joints i and j are immediate neighbors in the kinematic tree, 0 otherwise), and $\Delta p_{ij}(t)$ the inter-joint

displacement vector:

$$\begin{aligned} \mathcal{L}_{\text{local-match}} = & \sum_t \sum_{i \neq j} m_{ij} \underbrace{\|\Delta p_{ij}^{\text{SMPL-X}}(t) - \Delta p_{ij}^{\text{Humanoid}}(t)\|_2^2}_{\text{position}} \\ & + \sum_t \sum_{i \neq j} m_{ij} \underbrace{(1 - \langle \Delta p_{ij}^{\text{SMPL-X}}(t), \Delta p_{ij}^{\text{Humanoid}}(t) \rangle)}_{\text{orientation}} \end{aligned} \quad (5)$$

where $p_i^{\text{SMPL-X}}(t)$ and $p_i^{\text{Humanoid}}(t)$ denote the global 3D position of joint i at time t , and Δp_{ij} denotes the position difference between joints i and j .

Smoothness Loss. To produce temporally smooth motions, we penalize the second-order finite difference of joint velocities \dot{q}_t and root translations $\dot{\gamma}_t$:

$$\mathcal{L}_{\text{smooth}} = \sum_t \|\dot{q}_t - 2\dot{q}_{t+1} + \dot{q}_{t+2}\|_1 + \sum_t \|\dot{\gamma}_t - 2\dot{\gamma}_{t+1} + \dot{\gamma}_{t+2}\|_1 \quad (6)$$

The overall fidelity loss is:

$$\mathcal{L}_{\text{Fidelity}} = w_{\text{global-match}} \mathcal{L}_{\text{global-match}} + w_{\text{local-match}} \mathcal{L}_{\text{local-match}} + w_{\text{smooth}} \mathcal{L}_{\text{smooth}} \quad (7)$$

B.1.2 Joint Feasibility Loss

The joint feasibility loss $\mathcal{L}_{\text{Feasibility}}$ penalizes joint configurations that approach or exceed the humanoid’s operational limits. It consists of a position-violation term and a velocity-violation term:

Position Violation. We penalize joint angles q_t that exceed 98% of the allowable range $[q_{\min}, q_{\max}]$:

$$\mathcal{L}_{\text{pos-violation}} = \sum_t [\max(0, q_t - 0.98q_{\max}) + \max(0, 0.98q_{\min} - q_t)] \quad (8)$$

Velocity Violation. Similarly, we penalize joint velocities \dot{q}_t that exceed 98% of the velocity limits $[\dot{q}_{\min}, \dot{q}_{\max}]$:

$$\mathcal{L}_{\text{vel-violation}} = \sum_t [\max(0, \dot{q}_t - 0.98\dot{q}_{\max}) + \max(0, 0.98\dot{q}_{\min} - \dot{q}_t)] \quad (9)$$

The overall joint feasibility loss is:

$$\mathcal{L}_{\text{Feasibility}} = \mathcal{L}_{\text{pos-violation}} + \mathcal{L}_{\text{vel-violation}} \quad (10)$$

B.1.3 Grounding Loss

The grounding loss corrects for floating or penetration artifacts by enforcing that the foot regions remain on the ground plane during frames with detected contact:

$$\mathcal{L}_{\text{Ground}} = \sum_{i \in \{\text{LH,LT,RH,RT}\}} \sum_t c_t^i \|p_t^i(z)\|_2^2 \quad (11)$$

where c_t^i is the ground-contact ratio for foot regions Left Heel (LH), Left Toe (LT), Right Heel (RH), and Right Toe (RT) at frame t , obtained as in the foot-contact filtering of Appendix A.1.3, and $p_t^i(z)$ is the vertical position of region i at frame t .

B.1.4 Skating Loss

The skating loss prevents foot sliding by penalizing the horizontal velocity of any foot region that is in contact with the ground:

$$\mathcal{L}_{\text{Skate}} = \sum_{i \in \{\text{LH,LT,RH,RT}\}} \sum_t c_t^i \|\dot{p}_t^i(x, y)\|_2 \quad (12)$$

where c_t^i is the same ground-contact ratio as in the grounding loss, and $\dot{p}_t^i(x, y)$ is the horizontal velocity of region i at frame t .

B.2 Comparison of Retargeting Methods

To provide an intuitive comparison of different retargeting approaches, we present qualitative results in Figure 9. Using a walking motion as an example, we demonstrate the distinct characteristics and limitations of each method.

Traditional inverse kinematics (IK) prioritizes matching end-effector positions, such as hands and feet, from rigidly scaled human motions. However, this approach produces unnatural locomotion patterns where the humanoid appears to walk on a tightrope rather than exhibiting a natural human-like gait. This occurs because the fixed scaling cannot account for the proportional differences between human and robot morphologies.

Shape-adaptive inverse kinematics (SINK) generates more natural-looking walking motions compared to traditional IK by optimizing body proportions. However, SINK suffers from physical violations that compromise motion realism. Common issues include foot penetration through the ground surface and fixed ankle angles that result from the lack of explicit contact constraints during the retargeting process.

In contrast, our proposed PhysSINK method achieves both natural movement patterns and physical reliability. The resulting motions maintain appropriate ankle angles while ensuring proper ground contact, demonstrating that PhysSINK successfully balances motion naturalness with physical constraints. This improvement stems from the incorporation of explicit physical constraint terms in the optimization objective.

We further compare GMR [69], an optimization-based IK approach, with PhysSINK. The two differ in how they generate the intermediate target motion. GMR scales the source motion by a heuristic: it estimates the subject’s height H_{src} from the first SMPL shape component (β), forms a ratio $r = H_{src}/H_{ref}$ to a reference height H_{ref} (e.g., 1.8m), and applies it to manually tuned per-limb scale factors. For a limb with relative position \mathbf{v}_{rel} from the pelvis and manual scale s_{limb} , the scaled target is $\mathbf{v}'_{target} = s_{limb} \times r \times \mathbf{v}_{rel}$, which a standard IK solver then tracks. PhysSINK instead optimizes the SMPL shape parameters (β) to match the humanoid in a shared T-pose and applies them to the original motion, preserving the original joint angles while adjusting limb lengths to the robot.

This difference matters for generalization. GMR’s linear scaling works for average-sized humans but fails on diverse body shapes (Figure 10): short subjects yield undersized targets that force the robot to crouch even when standing, while tall subjects yield oversized targets beyond its reach, causing locked knees and floating feet. By applying the original joint angles with a robot-matched shape, PhysSINK reproduces the intended motion regardless of the source subject’s proportions.

This also affects policy training. We retarget the PHUMA sources with GMR (excluding the pre-retargeted LaFAN1 [12] and LocoMuJoCo [21]) and train a MaskedMimic policy under the same setup. As shown in Table 9, the PhysSINK-retargeted policy outperforms it on both the PHUMA Test and Unseen Video benchmarks.

Table 9: **Imitation Performance: GMR vs. PhysSINK Retargeting on Unitree G1.** We evaluate the imitation performance of the MaskedMimic policy trained using datasets retargeted with GMR and PhysSINK on the Unitree G1.

Dataset	PHUMA Test					Unseen Video				
	Total	Stationary	Angular	Vertical	Horizontal	Total	Stationary	Angular	Vertical	Horizontal
GMR	84.0	92.1	77.8	77.1	89.1	75.2	99.1	77.8	61.7	52.7
PhysSINK	89.9	94.2	87.6	84.2	91.8	81.7	97.4	86.7	61.7	71.4

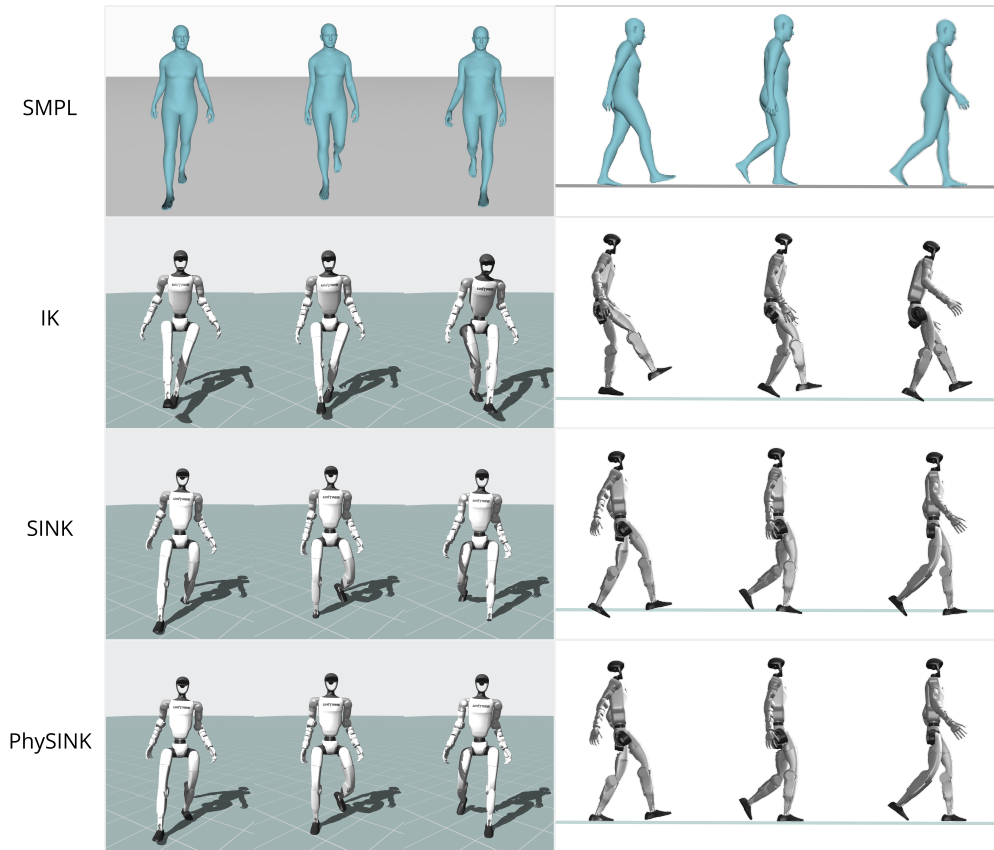


Figure 9: **Qualitative Comparison of Retargeting Methods.** This figure provides a visual comparison of human motion retargeted to a humanoid robot using the IK, SINK, and PhySINK methods. The top row shows the original human motion from the SMPL model, while the rows below show the resulting motions for each retargeting method.

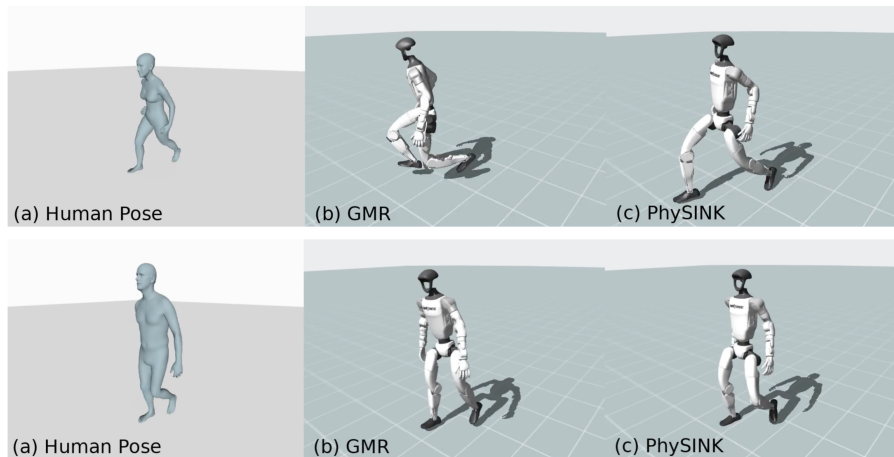


Figure 10: **Qualitative Comparison of Motion Retargeting: GMR vs. PhySINK.** Comparison showing the limitations of GMR when handling extreme human heights. The top row illustrates retargeting from a short subject, where GMR causes excessive motion compression and crouching. The bottom row illustrates retargeting from a tall subject, where GMR generates infeasible targets, resulting in artifacts like joint locking (e.g., rigid knees) and loss of ground contact. PhySINK maintains kinematic feasibility in both cases.

C Motion Imitation Learning

C.1 Observation Space Compositions

This section provides detailed information about the observation space composition used in our experimental setup, as summarized in Table 10 and Table 11. The observation space consists of two main components: proprioceptive states and goal states.

C.1.1 MaskedMimic

Proprioceptive States. The proprioceptive information includes root height, body positions, body rotations, body velocities, and body angular velocities. The Unitree G1 and H1-2 robots have 33 and 25 bodies, respectively. For body positions, the root body is excluded from the position measurements.

Goal States. The goal states comprise both relative and absolute body positions and rotations. The relative component represents the difference between the future 15 timesteps of reference motion states and the current proprioceptive state. The absolute component represents states relative to the reference motion’s root position, providing a root-relative coordinate frame for the target motion.

Table 10: **Observation Space Dimensions of MaskedMimic.**

State	Dimension	
	G1	H1-2
(a) Proprioceptive State		
Root height	1	1
Body position	32×3	24×3
Body rotation	33×6	25×6
Body velocity	33×3	25×3
Body angular velocity	33×3	25×3
(b) Goal State		
Relative body position	$33 \times 15 \times 3$	$25 \times 15 \times 3$
Absolute body position	$33 \times 15 \times 3$	$25 \times 15 \times 3$
Relative body rotation	$33 \times 15 \times 6$	$25 \times 15 \times 6$
Absolute body rotation	$33 \times 15 \times 6$	$25 \times 15 \times 6$
Time	$33 \times 15 \times 1$	$25 \times 15 \times 1$
Total dim	9898	7498

C.1.2 BeyondMimic

Proprioceptive States. The proprioceptive information includes the previous action, the base angular velocity in the body frame, and the DoF position and DoF velocity vectors.

Goal States. The goal states comprise an instantaneous component and a future component. The instantaneous component provides the reference motion’s DoF position, DoF velocity, and 6D torso orientation.

Unlike the original BeyondMimic, we augment the goal state with the reference motion’s future trajectory. At each future frame, we add the components listed in Table 11. We sample $K = 20$ such frames, linearly spaced over a horizon of $H = 95$ control steps (1.9 s at 50 Hz), forming a 20×78 tensor. A separate motion encoder then projects this tensor to a 128-D embedding, which is concatenated with the rest of the observation. Including this future component yields a substantially higher success rate than relying on the instantaneous goal alone, in both IsaacSim and MuJoCo and on both the PHUMA Test and Unseen Video splits (Table 12).

Table 11: **Observation Space Dimensions of BeyondMimic.**

State	Dimension (G1)
(a) Proprioceptive State	
Previous action	29
Base angular velocity	3
DoF position	29
DoF velocity	29
(b) Goal State	
(b.1) Instantaneous	
DoF position	29
DoF velocity	29
Torso rotation	6
(b.2) Future Motion Targets (motion-encoder input)	
Root height	20×1
Root roll/pitch	20×2
Base linear velocity	20×3
Base yaw rate	20×1
DoF position	20×29
Local key-body position	$20 \times 14 \times 3$
Total dim	282

Table 12: **Sim-to-Sim Results of PHUMA-trained BeyondMimic Policies.** This table demonstrates the effect of the future-trajectory observation on the policy for the Unitree G1, evaluated on the PHUMA Test and Unseen Video splits. SR is the whole-body success rate at 0.5 m (%); $E_{g\text{-mpjpe}}$, $E_{l\text{-mpjpe}}$, E_{acc} , and E_{vel} are tracking errors (mm), following the convention of [9, 11, 37] and averaged over successful motions.

Future	IsaacSim					MuJoCo				
	SR \uparrow	$E_{g\text{-mpjpe}} \downarrow$	$E_{l\text{-mpjpe}} \downarrow$	$E_{\text{acc}} \downarrow$	$E_{\text{vel}} \downarrow$	SR \uparrow	$E_{g\text{-mpjpe}} \downarrow$	$E_{l\text{-mpjpe}} \downarrow$	$E_{\text{acc}} \downarrow$	$E_{\text{vel}} \downarrow$
(a) PHUMA test										
\times	47.15	115.78	32.70	1.15	4.29	46.91	156.64	32.92	1.22	4.36
\checkmark	78.77	112.00	28.28	1.18	4.14	76.02	142.79	28.98	1.24	4.18
(b) Unseen Video										
\times	47.82	123.71	31.93	1.07	4.93	47.42	122.89	30.60	1.09	4.85
\checkmark	71.63	121.69	24.87	1.11	4.78	70.44	122.68	23.79	1.14	4.73

C.2 Reward Function

The reward function used for training the tracking policy consists of multiple components, as detailed in Table 13 and Table 14. The overall reward structure comprises two main categories: motion tracking task rewards and regularization rewards.

C.2.1 MaskedMimic

Motion Tracking Rewards. These components encourage the policy to match the reference motion by providing higher rewards when the robot’s proprioceptive states closely resemble the target motion states.

Regularization Rewards. To promote smooth and stable motion execution, we include regularization terms that penalize undesirable behaviors. Specifically, we augment the standard MaskedMimic reward formulation with action rate penalties that discourage large changes between consecutive actions, helping to ensure smooth joint movements and prevent abrupt motion transitions.

Table 13: **Reward Function Terms of MaskedMimic.**

Term	Expression	Weight
(a) Task		
Global body position	$\exp(-100 \cdot \ p_t - \hat{p}_t\ _2^2)$	0.5
Root height	$\exp(-100 \cdot (h_t^{\text{root}} - \hat{h}_t^{\text{root}})^2)$	0.2
Global body rotation	$\exp(-10 \cdot \ \theta_t \ominus \hat{\theta}_t\ _2^2)$	0.3
Global body velocity	$\exp(-0.5 \cdot \ v_t - \hat{v}_t\ _2^2)$	0.1
Global body angular velocity	$\exp(-0.1 \cdot \ \omega_t - \hat{\omega}_t\ _2^2)$	0.1
(b) Regularization		
Power consumption	$\ F \odot \dot{q}\ _1$	-1e-05
Action rate	$\ a_t - a_{t-1}\ _2^2$	-0.2

C.2.2 BeyondMimic

Motion Tracking Rewards. BeyondMimic decomposes motion tracking into two components: tracking the global reference motion (position, rotation, and linear/angular velocity), and tracking the relative reference motion, which factors out the root’s global horizontal translation (and heading) and re-anchors the body targets to the robot’s own root.

Regularization Rewards. To promote smooth and stable motion execution we use the same regularization terms used in BeyondMimic as in Table 14.

Table 14: **Reward Function Terms of BeyondMimic.**

Term	Expression	Weight
(a) Motion Tracking		
Reference body position	$\exp(-\ p_t^{\text{ref}} - \hat{p}_t^{\text{ref}}\ _2^2 / 0.3^2)$	0.5
Reference body rotation	$\exp(-\ \theta_t^{\text{ref}} \ominus \hat{\theta}_t^{\text{ref}}\ _2^2 / 0.4^2)$	0.5
Global body linear velocity	$\exp(-\frac{1}{B} \sum_b \ v_t^b - \hat{v}_t^b\ _2^2 / 1.0^2)$	1.0
Global body angular velocity	$\exp(-\frac{1}{B} \sum_b \ \omega_t^b - \hat{\omega}_t^b\ _2^2 / \pi^2)$	1.0
Relative body position	$\exp(-\frac{1}{B} \sum_b \ p_t^b - \hat{p}_t^b\ _2^2 / 0.3^2)$	1.0
Relative body rotation	$\exp(-\frac{1}{B} \sum_b \ \theta_t^b \ominus \hat{\theta}_t^b\ _2^2 / 0.4^2)$	1.0
(b) Regularization		
Action rate	$\ a_t - a_{t-1}\ _2^2$	-0.1
DoF position-limit violation	$\sum_j (\text{ReLU}(q_t^j - q_{\text{max},0.9}^j) + \text{ReLU}(q_{\text{min},0.9}^j - q_t^j))$	-100
Undesired contacts	$\sum_b \mathbf{1}[\ F_t^b\ _2 > 1 \text{ N}]$	-0.5

C.3 PPO Hyperparameters

The detailed hyperparameter configurations used for PPO training in MaskedMimic and BeyondMimic are provided in Table 15 and Table 16, respectively.

C.4 Domain Randomization

To bridge the simulation-to-reality gap and improve robustness to model and sensor inaccuracies, we apply domain randomization during training. The complete set of randomized parameters is summarized in Table 17.

Table 15: **PPO Hyperparameter Values for Model Training of MaskedMimic.**

Hyperparameter	Value
Optimizer	Adam
Num envs	8192
Mini Batches	32
Learning epochs	1
Entropy coefficient	0.0
Value loss coefficient	0.5
Clip param	0.2
Max grad norm	50.0
Init noise std	-2.9
Actor learning rate	2e-5
Critic learning rate	1e-4
GAE decay factor(λ)	0.95
GAE discount factor(γ)	0.99
Actor Transformer dimension	512
Actor layers	4
Actor heads	4
Critic MLP size	[1024, 1024, 1024, 1024]
Activation	ReLU

Table 16: **PPO Hyperparameter Values for Model Training of BeyondMimic.**

Hyperparameter	Value
Optimizer	AdamW
Num envs	8192
Steps per env	24
Mini batches	4
Learning epochs	8
Entropy coefficient	0.005
Value loss coefficient	1.0
Clip param	0.2
Max grad norm	1.0
Init noise std	1.0
Actor learning rate	1e-5
Critic learning rate	1e-5
GAE decay factor(λ)	0.95
GAE discount factor(γ)	0.99
Actor MLP size	[768, 512, 256]
Critic MLP size	[768, 512, 256]
Motion encoder hidden dim	60
Motion encoder output dim	128
Activation	SiLU

C.4.1 BeyondMimic

We adopt the domain randomization scheme of BeyondMimic [18], covering actuator gains, base inertial properties, contact properties, external pushes, initial-pose perturbations, and observation noise. Noise is added only to the actor observation stream; the critic stream is noise-free. All randomization and noise are disabled at evaluation time. The exact ranges and schedules are listed in Table 17.

Table 17: **Domain Randomization Ranges of BeyondMimic.**

Parameter	Range
P-gain scale s_P	$\mathcal{U}(0.9, 1.1)$
D-gain scale s_D	$\mathcal{U}(0.9, 1.1)$
DoF position bias	$\mathcal{U}(-0.025, 0.025)$ rad
Base CoM offset x	$\mathcal{U}(-0.025, 0.025)$ m
Base CoM offset y, z	$\mathcal{U}(-0.05, 0.05)$ m
Static friction	$\mathcal{U}(0.3, 1.6)$
Dynamic friction	$\mathcal{U}(0.3, 1.2)$
Restitution	$\mathcal{U}(0.0, 0.5)$
Push interval	$\mathcal{U}(1.0, 3.0)$ s
Push linear velocity	$\mathcal{U}(\pm 0.5, \pm 0.5, \pm 0.2)$ m/s
Push angular velocity	$\mathcal{U}(\pm 0.52, \pm 0.52, \pm 0.78)$ rad/s
Initial DoF position	$\mathcal{U}(-0.1, 0.1)$ rad
Initial root position	$\mathcal{U}(\pm 0.05, \pm 0.05, \pm 0.01)$ m
Initial root rotation	$\mathcal{U}(\pm 0.1, \pm 0.1, \pm 0.2)$ rad
Initial root linear vel.	$\mathcal{U}(\pm 0.1, \pm 0.1, \pm 0.05)$ m/s
Initial root angular vel.	$\mathcal{U}(\pm 0.1, \pm 0.1, \pm 0.1)$ rad/s
Obs. noise: base angular vel. (σ)	0.2 rad/s
Obs. noise: DoF position (σ)	0.01 rad
Obs. noise: DoF velocity (σ)	0.5 rad/s
Obs. noise: motion ref orientation (σ)	0.05

D Experiment Details

D.1 Self-Collected Video Dataset

To ensure fair evaluation of imitation performance on unseen motions, we create a custom evaluation dataset using self-collected video recordings. This dataset contains motions uniformly distributed across the 11 motion types shown in Figure 8b, providing balanced coverage for comprehensive performance assessment.

The dataset creation process follows three main steps: (1) recording videos of human performers executing each motion type, (2) converting videos into SMPL human motion parameters using a video-to-motion model, and (3) retargeting the human motions to humanoid robot motions using our PhySINK method.

First, we record videos covering all 11 motion categories, collecting a uniform distribution for each type. We then apply the TRAM video-to-motion model [24] to extract SMPL motion parameters from the recorded videos. Finally, we process these SMPL motions with PhySINK retargeting to generate physically reliable humanoid motions. Example results from this dataset are illustrated in Figure 11.

This self-collected evaluation set ensures that our performance assessments are conducted on completely unseen motions that were not influenced by any training data sources, providing an unbiased evaluation of generalization capabilities.

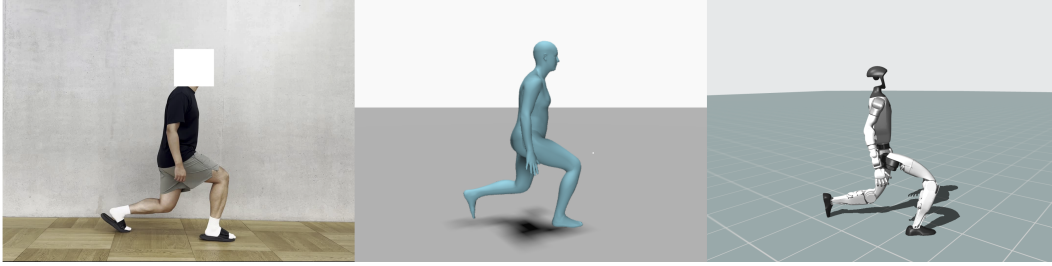


Figure 11: **Overview of the Self-collected Data Pipeline.** This figure illustrates the three main steps of our data collection pipeline: (left) a self-recorded video of a human motion, (center) the motion extracted using a video-to-motion model, and (right) the final motion retargeted to a humanoid robot.

D.2 Success Rate Threshold Analysis

To demonstrate the limitations of the conventional success rate threshold, we evaluate imitation performance using both the standard 0.5m threshold and our proposed stricter 0.15m threshold. This comparison reveals the true quality differences between policies trained on different datasets.

Tables 18 and 19 present the results for both threshold settings. Under the loose 0.5m threshold, policies trained on different datasets show relatively similar success rates, with differences appearing modest. However, when evaluated with the stricter 0.15m threshold, performance differences become substantially more pronounced.

These results confirm that PHUMA-trained policies achieve more precise motion tracking, producing imitations that remain accurate even under stringent evaluation criteria. The threshold analysis validates our choice to adopt the 0.15m threshold as a more meaningful measure of imitation quality.

Table 18: **Performance Comparison based on Success Threshold in PHUMA Test.**

Dataset	Hours	Success Threshold=0.15m					Success Threshold=0.5m				
		Total	Stationary	Angular	Vertical	Horizontal	Total	Stationary	Angular	Vertical	Horizontal
(a) G1											
LaFAN1	2.4	46.1	66.1	36.2	24.0	42.5	74.8	87.8	69.2	47.1	72.6
AMASS	20.9	76.2	88.5	72.1	56.8	66.8	90.2	95.0	87.9	81.1	83.7
Humanoid-X	231.4	50.6	78.4	43.0	26.0	31.8	78.4	91.3	72.9	59.5	65.9
PHUMA	73.0	92.7	95.6	91.7	86.0	85.6	97.1	98.7	96.5	94.4	92.5
(b) H1-2											
LaFAN1	2.4	62.0	79.3	54.7	26.6	58.9	70.8	92.4	66.7	56.4	68.2
AMASS	20.9	54.4	74.9	45.9	17.2	49.6	70.4	86.3	62.6	41.4	65.9
Humanoid-X	231.4	49.7	74.6	40.4	17.0	37.3	54.8	78.5	45.2	22.1	43.2
PHUMA	73.0	82.7	91.5	79.5	68.1	68.4	92.0	96.6	89.7	85.6	79.4

Table 19: **Performance Comparison based on Success Threshold in Unseen Video.**

Dataset	Hours	Success Threshold=0.15m					Success Threshold=0.5m				
		Total	Stationary	Angular	Vertical	Horizontal	Total	Stationary	Angular	Vertical	Horizontal
(a) G1											
LaFAN1	2.4	28.4	46.9	28.4	19.6	10.5	78.2	85.5	70.8	76.3	80.8
AMASS	20.9	70.2	90.7	75.0	62.7	44.1	92.3	99.2	92.1	82.1	88.0
Humanoid-X	231.4	39.1	78.0	39.6	23.0	6.5	84.1	98.3	79.9	76.0	76.2
PHUMA	73.0	82.9	96.7	88.0	71.8	67.1	93.7	100.0	96.8	85.9	84.7
(b) H1-2											
LaFAN1	2.4	70.8	92.4	66.7	56.4	68.2	85.5	97.5	79.0	77.5	90.0
AMASS	20.9	64.3	87.3	59.7	46.0	63.9	80.4	93.3	69.9	72.8	89.0
Humanoid-X	231.4	60.5	88.3	60.0	48.7	39.7	68.7	93.3	65.1	60.2	50.5
PHUMA	73.0	78.6	97.5	76.8	74.5	63.8	89.9	99.2	89.4	84.6	83.9

D.3 Cross-Simulator Generalization Analysis

To evaluate whether PHUMA benefits cross-simulator transfer, we also trained the KungfuBot [86] policy in Isaac Gym. We compared two training configurations: one using AMASS with SINK retargeting and another using PHUMA. For both configurations, we followed the standard KungfuBot [86] teacher-student training pipeline and evaluation metrics. Tables 20 and 21 present the teacher and student policy performance in the training simulator (Isaac Gym). The results show that policies trained with PHUMA achieve superior imitation performance, demonstrating that PHUMA’s benefits extend to other motion imitation algorithms. Importantly, this performance advantage also transfers to the evaluation simulator. Table 22 shows the zero-shot performance in MuJoCo, where the PHUMA-trained policy maintains its superiority across motion categories, indicating robust cross-simulator generalization.

Table 20: **Imitation Performance of the KungfuBot Teacher Policy in Isaac Gym.** We evaluate the imitation performance of KungfuBot teacher policy with unseen motions on the Unitree G1.

Dataset	PHUMA Test					Unseen Video				
	Total	Stationary	Angular	Vertical	Horizontal	Total	Stationary	Angular	Vertical	Horizontal
AMASS	77.8	90.8	71.2	58.3	84.7	83.5	100.0	83.3	74.5	72.5
PHUMA	91.0	96.4	88.3	87.6	90.5	87.1	99.1	89.2	77.7	76.9

Table 21: **Imitation Performance of the KungfuBot Student Policy in Isaac Gym.** We evaluate the imitation performance of KungfuBot student policy with unseen motions on the Unitree G1.

Dataset	PHUMA Test					Unseen Video				
	Total	Stationary	Angular	Vertical	Horizontal	Total	Stationary	Angular	Vertical	Horizontal
AMASS	66.6	86.7	58.8	41.8	68.4	67.7	97.4	68.0	59.6	37.4
PHUMA	82.9	93.5	78.5	74.2	81.7	73.8	97.4	76.9	63.8	47.3

Table 22: **Sim-to-Sim transfer performance across motion dataset.** We evaluate the zero-shot motion tracking success rate of policies trained on PHUMA and AMASS when transferred from the source simulator (Isaac Gym) to the target simulator (MuJoCo). The results are demonstrated on the G1 humanoid to assess robustness against domain shifts in physics engines.

Dataset	PHUMA Test					Unseen Video				
	Total	Stationary	Angular	Vertical	Horizontal	Total	Stationary	Angular	Vertical	Horizontal
AMASS	62.1	81.4	54.2	38.8	64.3	64.3	86.2	68.5	54.3	37.4
PHUMA	75.0	87.6	69.3	61.6	76.3	70.0	87.9	78.8	59.6	38.5

E Ablation Studies

E.1 Mocap only and Video only data performance

To analyze the influence of the human motion source on the downstream motion tracking policy, we divide the PHUMA dataset into two distinct subsets: motions derived from motion capture (Mocap) and motions derived from video-to-motion estimation (Video-Sourced).

We leverage these subsets to train the MaskedMimic policy using identical hyperparameters in Section C. As demonstrated in Table 24, the policy trained with video-sourced PHUMA consistently yielded superior imitation performance across all motion categories compared to the policy trained with the mocap-sourced subset.

We attribute this result primarily to the significantly larger and broader motion distribution of the video-sourced data. As illustrated in Figure 8a, the video-sourced dataset covers a much broader range of motion types and contains nearly two times more data than the mocap-sourced dataset. Furthermore, as shown in Table 23, the PhysSINK retargeting method ensures competitive motion quality for both subsets. Because the retargeting quality is similar, the dominant factor leading to the higher imitation performance is the larger size and greater diversity of the video-sourced dataset.

Table 23: **Performance Evaluation of PHUMA based on Data Source (MoCap vs. Video)**. We present a quantitative comparison evaluating the performance achieved using PHUMA data derived from motion capture (MoCap) versus video, concluding that both sources offer competitive results.

	Motion Fidelity (%)	Joint Feasibility (%)	Non-Floating (%)	Non-Penetration (%)	Non-Skating (%)
MoCap	96.7	100.0	99.9	94.3	92.1
Video	93.8	100.0	99.9	98.0	88.3

Table 24: **Imitation Performance of PHUMA based on Data Source (MoCap vs. Video)**. We evaluate the imitation performance of MaskedMimic policy trained with PHUMA data derived from motion capture (MoCap) versus video on the Unitree G1.

Dataset	PHUMA Test					Unseen Video				
	Total	Stationary	Angular	Vertical	Horizontal	Total	Stationary	Angular	Vertical	Horizontal
MoCap	75.2	88.2	68.4	49.0	86.9	73.0	96.6	73.9	56.4	58.2
Video	85.7	92.9	81.8	75.5	89.5	76.2	100.0	76.4	59.6	62.6

E.2 Physics-based Filtering

This section provides ablation studies on the physics-based filtering criteria used in data curation (Table 7) and the physics-constrained losses used in PhySINK.

E.2.1 Data Distribution Based on Physics-based Filtering

Figure 12 shows the filtering statistics when sequentially applying the physics-based criteria from Table 7 to Humanoid-X [1]. The filters are applied in the following order: (1) root jerk filter (jerk $< 50 \text{ m/s}^3$), (2) contact filter (foot contact score > 0.6), (3) height filter (minimum pelvis height $> 0.6 \text{ m}$ and maximum pelvis height $< 1.5 \text{ m}$), and (4) base of support (BoS) filter (pelvis distance to BoS $< 6 \text{ cm}$ and spine1 distance to BoS $< 11 \text{ cm}$). After applying all filters sequentially, 27.1% of the original Humanoid-X dataset remains, representing motions that satisfy physical plausibility constraints.

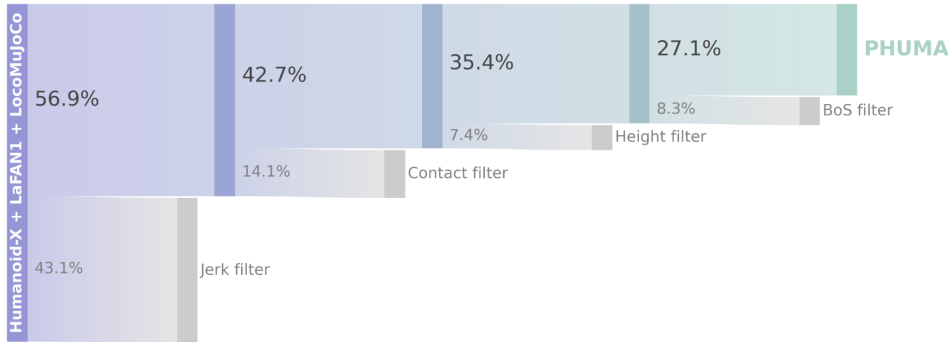


Figure 12: **Dataset Statistics After Physics-based Filtering**. Distribution of motion sequences after applying physics-based filtering to the combined Humanoid-X, LaFAN1, and LocoMuJoCo datasets.

E.2.2 PhySINK’s Robustness to Noisy Motion Sources

To evaluate how robustly PhySINK handles noisy human motion inputs, we retarget Humanoid-X motion sources with varying levels of filtering: (1) raw Humanoid-X (no filtering), (2) Humanoid-X + jerk filtering, (3) Humanoid-X + foot contact filtering, (4) Humanoid-X + height filtering, (5) Humanoid-X + BoS filtering, and (6) Humanoid-X + all filters. We then apply PhySINK to each variant. Note that we exclude pre-retargeted datasets (LaFAN1 and LocoMuJoCo) from this analysis to isolate the effect of filtering on Humanoid-X. As shown in Table 25, PhySINK demonstrates

Table 25: **PhySINK Retargeting Robustness to Noisy Motion Sources.** This figure presents an experiment to evaluate how robustly the PhySINK method retargets various noisy Humanoid-X motion sources. The six distinct motion source groups used for retargeting are compared: (1) Original Humanoid-X, and Humanoid-X motion sources sequentially refined by applying (2) Jerk filtering, (3) Foot Contact filtering, (4) Height filtering, (5) BoS filtering, and (6) All filtering (PHUMA).

Motion Source	Hours	Motion Fidelity (%)	Joint Feasibility (%)	Non-Floating (%)	Non-Penetration (%)	Non-Skating (%)
Humanoid-X	237.2	70.6	100.0	98.7	92.2	90.1
Jerk Filter	141.1	76.9	100.0	99.7	96.5	92.0
Foot Contact Filter	123.1	77.1	100.0	99.8	96.8	90.6
Height Filter	135.7	87.0	100.0	99.4	94.7	89.8
BoS Filter	110.3	90.7	100.0	99.4	94.9	90.0
All Filter	62.2	94.8	100.0	99.9	96.7	89.7

robust retargeting performance across motion sources with varying noise levels, successfully handling physical implausibilities present in the raw data.

E.3 Impact of Motion Retargeting Quality on Policy Performance

To investigate how physical artifacts in retargeted motion data affect policy learning, we train MaskedMimic policies on datasets generated using six retargeting methods with varying artifact levels. The methods are: (1) **IK**, which produces significant artifacts in motion fidelity, joint limits, grounding, and skating; (2) **GMR**, which reduces motion fidelity loss, grounding issues, and skating compared to IK; (3) **SINK**, which improves motion fidelity and joint limit violations; (4) **SINK + Joint Feasibility Loss**, which further reduces joint limit violations; (5) **SINK + Joint Feasibility + Grounding Loss**, which addresses all artifact types except skating; and (6) **PhySINK**, which minimizes all physical artifacts. To isolate the effect of retargeting quality, we exclude the LaFAN1 and LocoMuJoCo datasets from this analysis, as they were pre-retargeted and would not allow for fair comparison across methods.

In Table 26, our results show that SINK-based methods, which first optimize the humanoid body shape before applying it to the original motion, consistently outperform IK-based methods that rely on heuristic scaling to bridge human-humanoid discrepancies. Notably, GMR achieves better performance than IK despite having similar joint limit issues, while the SINK variants further outperform GMR in tracking performance. However, across the SINK variants themselves (SINK, SINK + Joint Feasibility Loss, SINK + Joint Feasibility + Grounding Loss), we observe comparable performance despite their similar levels of motion fidelity, joint feasibility, and grounding quality, the main differences among these variants being penetration and skating artifacts.

These results indicate that motion fidelity is the most critical factor affecting motion tracking performance. The substantial performance improvement of GMR over IK (achieved primarily through motion fidelity gains rather than joint feasibility improvements) demonstrates that preserving motion fidelity during retargeting has a greater impact on policy learning than other artifact types. However, once motion fidelity reaches a certain threshold (as in the SINK variants), further reductions in other artifact types yield diminishing returns for policy learning.

Table 26: **Ablation Studies of Imitation Performance on Retargeting Loss.** We evaluate the imitation performance of MaskedMimic policies trained with and without the physical constraint loss (Table 1) using the Unitree G1 robot.

Dataset	PHUMA Test					Unseen Video				
	Total	Stationary	Angular	Vertical	Horizontal	Total	Stationary	Angular	Vertical	Horizontal
IK	70.5	85.9	63.3	47.6	77.3	68.5	96.6	72.4	43.6	49.5
GMR	84.0	92.1	77.8	77.1	89.1	75.2	99.1	77.8	61.7	52.7
SINK	89.1	94.0	86.0	84.9	90.7	79.0	100.0	81.8	62.8	62.6
+ Joint Feasibility Loss	87.0	92.1	83.6	79.8	90.9	78.6	94.8	84.7	56.4	67.0
+ Grounding Loss	90.0	93.5	87.9	85.6	92.0	80.4	98.3	86.2	60.6	64.8
+ Skating Loss	89.9	94.2	87.6	84.2	91.8	81.7	97.4	86.7	61.7	71.4

F Pelvis-Only Path Following Control Performance

We evaluate whether training on PHUMA enables better pelvis path-following control compared to the AMASS dataset. Using MaskedMimic’s partially-constrained protocol, we train two student policies: one distilled from an AMASS-trained teacher and another from a PHUMA-trained teacher. Both students receive only pelvis position and rotation as input.

As shown in Table 27, policies trained on PHUMA outperform those trained on baseline datasets across all motion categories and humanoids, with the largest gap on dynamic motions. Figure 13 illustrates this, where AMASS-trained policies fail on running while PHUMA-trained policies remain robust.

Table 27: **Pelvis path following performance across motion dataset.** We evaluate the success rate of pelvis path-following control for policies trained on the AMASS and PHUMA datasets across various pelvis trajectories from the PHUMA Test and Unseen Video.

Dataset	PHUMA Test					Unseen Video				
	Total	Stationary	Angular	Vertical	Horizontal	Total	Stationary	Angular	Vertical	Horizontal
(a) G1										
AMASS	60.5	85.6	60.1	51.4	66.5	54.8	83.6	66.5	33.0	27.5
PHUMA	84.5	94.6	86.1	83.7	90.2	74.6	98.3	83.3	54.3	57.1
(a) H1-2										
AMASS	60.4	84.0	62.8	43.6	78.7	72.3	96.6	77.3	52.1	72.5
PHUMA	73.9	91.2	76.5	66.9	84.8	78.1	96.6	77.8	60.6	78.0

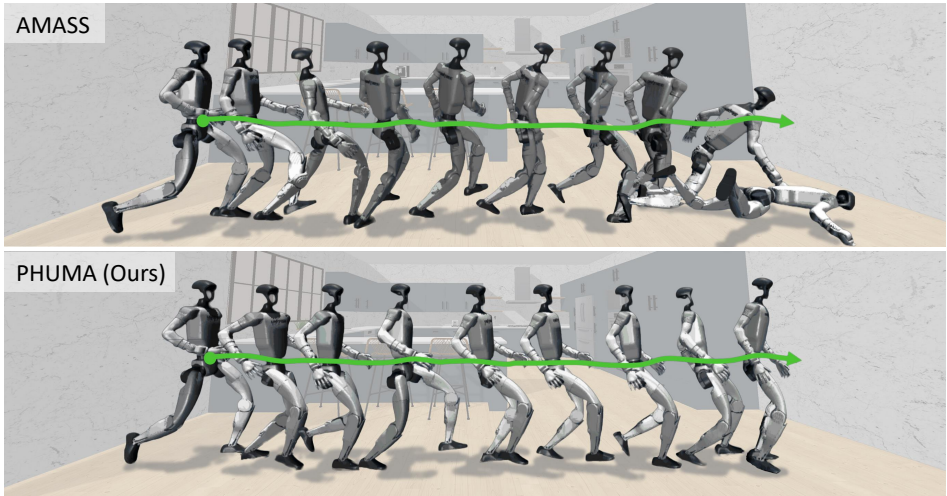


Figure 13: **Path following on running motion.** We visualize the robot’s trajectory in a running motion. The target pelvis path is visualized with a green line. Top row presents results from a policy trained on AMASS, while bottom row presents results from a policy trained on PHUMA.

G Results on H1-2 Robot

This appendix provides complete results on the Unitree H1-2 [82] robot, complementing the G1 results presented in the main text.

G.1 PhySINK Ablation on H1-2

Table 28 presents the ablation study of PhySINK retargeting on the H1-2 humanoid robot, showing the progressive impact of each physical constraint loss.

Table 28: **Quantitative comparison and ablation study of retargeting methods on H1-2.** Progressive impact of adding each physical constraint loss.

	Motion Fidelity (%)	Joint Feasibility (%)	Non-Floating (%)	Non-Penetration (%)	Non-Skating (%)
IK	36.3	80.9	57.7	45.2	56.1
GMR	58.0	71.8	6.0	100.0	62.3
SINK	93.9	15.3	42.2	81.4	47.9
+ Joint Feasibility Loss	94.0	99.5	44.4	79.9	50.7
+ Grounding Loss	93.9	99.9	99.8	98.1	49.3
+ Skating Loss = PhySINK	93.9	99.9	97.7	99.7	87.7

G.2 Retargeting Method Comparison on H1-2

Table 29 shows motion tracking performance across retargeting approaches on the H1-2 robot.

Table 29: **Motion tracking performance across retargeting approaches on H1-2.** Success rates using two test sets.

Retarget	PHUMA Test					Unseen Video				
	Total	Stationary	Angular	Vertical	Horizontal	Total	Stationary	Angular	Vertical	Horizontal
IK	45.3	70.9	35.7	15.2	35.0	54.2	78.0	60.7	30.1	28.6
GMR	56.6	75.7	48.1	24.8	65.9	64.3	80.2	65.5	52.1	53.8
SINK	54.4	74.9	45.9	17.2	49.6	64.3	87.3	59.7	46.0	63.9
PhySINK	64.3	83.6	57.0	27.7	55.9	72.4	99.2	66.3	57.4	63.1

G.3 Dataset Effectiveness on H1-2

Table 30 presents motion tracking performance across training datasets on the H1-2 robot.

Table 30: **Motion tracking performance across datasets on H1-2.** Success rates evaluated on two test sets.

Dataset	Hours	PHUMA Test					Unseen Video				
		Total	Stationary	Angular	Vertical	Horizontal	Total	Stationary	Angular	Vertical	Horizontal
LaFAN1	2.4	62.0	79.3	54.7	26.6	58.9	70.8	92.4	66.7	56.4	68.2
AMASS	20.9	54.4	74.9	45.9	17.2	49.6	64.3	87.3	59.7	46.0	63.9
Humanoid-X	231.4	49.7	74.6	40.4	17.0	37.3	60.5	88.3	60.0	48.7	39.7
PHUMA	73.0	82.7	91.5	79.5	68.1	68.4	78.6	97.5	76.8	74.5	63.8